JOURNAL OF COMPUTATIONAL PHYSICS **145,** 575–610 (1998)
ARTICLE NO. CP986037

Rankine–Hugoniot–Riemann Solver Considering Source Terms and Multidimensional Effects

P. Jenny* and B. Müller†

**Sibley School of Mechanical and Aerospace Engineering, Cornell University, Ithaca, New York 14853; and †Department of Mathematics, Lulea University of Technology, 97187, Lulea, Sweden*
E-mail: jenny@mae.cornell.edu

Received June 19, 1997; revised May 28, 1998

A new approach for a flux solver is introduced, which takes into account source terms, viscous terms, and multidimensional effects. The basic idea is to distribute the source terms, which also contain the viscous terms and multidimensional effects, from the cells to the cell interfaces. Then the fluxes on both sides of a cell interface are determined by the Rankine–Hugoniot conditions and a linearized Riemann solver. The resulting Rankine–Hugoniot–Riemann (RHR) solver yields much more accurate results than conventional Riemann solvers for steady premixed laminar flames in 1D and 2D and a steady 2D inviscid channel flow with injection. Unsteady flow simulations of two colliding flames producing sound and of acoustic oscillations flattening a 2D Bunsen flame demonstrate that the new flux solver is able to compute acoustic effects in flames accurately. This approach for a flux solver is more general and can also be applied to solve other partial differential equations which can be expressed as hyperbolic systems with source terms ex- or including higher spatial derivatives, e.g., for the shallow water equations and for the magnetohydrodynamical equations.

1. INTRODUCTION

In recent years, the development of numerical methods for combustion problems has been driven by an increasing industrial demand for fast and accurate computations of reacting flow [21]. Considering the interaction of acoustics and combustion adds another level of complexity. However, the control of thermoacoustic instabilities is decisive for the safe operation of rocket motors and modern gas turbines [13]. Therefore, we have started to develop a numerical method for the investigation of thermoacoustics and to apply it to the computation of acoustic effects in premixed laminar flames. These flames are characterized by low Mach numbers of $O(10^{-3})$ and small pressure changes of a few Pa. Interactions

0021-9991/98 $25.00

between acoustics and flames are governed by the compressible Navier–Stokes equations for reacting gas mixtures with source terms describing chemical and heat release rates [15]. Considering acoustics for low Mach numbers M means a drastic time step reduction of $O(M)$ compared to solving the low Mach number equations, which allow for arbitrary temperature and density changes but from which acoustics is removed [23, 7].

Before presenting our new numerical approach to simulate thermoacoustics, we shall briefly review existing methods for computing related problems governed by non-homogeneous conservation laws. When computing stiff reaction waves, the spatial and temporal resolution has to be chosen sufficiently high to avoid non-physical wave speeds. These waves have the structure of a fluid dynamic shock that raises the pressure to some peak value, followed immediately by a reaction zone that brings the pressure back down to a new equilibrium value. On coarse grids it is not possible to resolve this combustion spike and for stiff source terms the numerical wave speed is totally wrong unless the space step is made extremely small. Examples and analyses of the numerical simulation of that problem are given by Oran and Boris [21], LeVeque and Yee [17], Lindström [20], and Klingenstein [14].

Chorin [3] analyzes the random choice method by Glimm, shows its usefulness for reacting flow, and carries out applications in one dimensional time-dependent reacting flow. In this method the solution is first approximated by a piecewise constant function at each time step. It is then advanced in time exactly and new values on the mesh are obtained by sampling. The advantage of this procedure is that the interaction of the flow and the chemical reaction can be taken into account when the Riemann problem is solved.

Roe [24] shows the necessity to modify the upwind schemes for non-homogeneous hyperbolic conservation laws. He approximates the integration along the characteristics taking the source terms into account and shows how to extend such schemes to higher order.

Sweby [29] points out that the TVD (total variation diminishing) property used in high resolution schemes for homogeneous conservation laws is inappropriate for problems with source terms. He utilizes a transformation of dependent variables to reduce the non-homogeneous problem to homogeneous form and suggests to apply the TVD scheme only to the fluxes of the homogeneous system and to treat the source term separately.

Bermudez and Vazquez [2] propose proper upwind discretizations of the source terms. They point out that conservativity is not guaranteed when solving the 1D shallow water equations with source terms although a conservative formulation is used. Therefore they introduce a conservation property. In [32] Vazquez extends this method to the 2D shallow water equations.

Colella [5] takes into account the tangential flux derivatives to construct the left and right states at the cell interfaces at the mid-time level. The resulting 1D Riemann problems normal to the cell interfaces are solved by Godunov's method to determine the normal fluxes. The tangential flux derivatives are approximated by Godunov's method as well.

Instead of increasing the resolution or upwinding the source terms, some authors have proposed flux discretizations, which take the source terms into account. LeVeque [18, 19] has developed a scheme where a flux jump at the volume center equals the source term. He shows very convincing solutions of the 1D and 2D shallow water equations.

In the present article, we present a new flux discretization which does not only take the source terms into account but also the viscous terms and multidimensional effects. Our approach was motivated by correcting a non-physical pressure peak and a large mass flow error when computing a steady premixed laminar flame using a conventional Riemann solver.

These numerical errors are not related to the ones appearing near contact discontinuities in gas mixture simulations with conservative schemes, if the gases on both sides of the interface have different temperature and different ratios of specific heats γ [12], because the errors in flames also occur, if γ is constant. Since the errors in flames even occur in 1D, they are neither related to similar numerical artifacts at moving shear waves [30]. Considering a simple model equation, we shall see that the numerical problems of conventional Riemann solvers for hyperbolic systems with source terms are caused by discretizing the inviscid fluxes, as if the equations were homogeneous. Most upwind schemes for the compressible Euler and Navier–Stokes equations are based on solving one dimensional Riemann problems at the cell interfaces and make use of conventional homogeneous Riemann solvers. As mentioned above, if such a conventional Riemann solver is applied to compute a steady premixed laminar flame, a non-physical peak in the pressure profile and a large error in the mass flow arise in the results, even if a conservative scheme without source term in the continuity equation is used [11]. These numerical phenomena become much more complex in higher space dimensions and exist also in a weaker form in 1D Navier–Stokes computations due to the viscous terms and in multidimensional homogeneous Euler simulations due to the multidimensional effects. In many flame computations such phenomena are reduced by using fine meshes and higher order schemes [8]. Generally these errors are negligible, but if acoustic phenomena in flames are to be simulated, they can become dominant. In spite of the importance only a few people seem to have studied the problems mentioned above and hardly any pressure plots of flames are published, except for [8].

To discretize the equations the cell centered finite volume method is used here. For the time integration the explicit Euler method is applied with an implicit treatment of the source term because of its stiffness. The basic idea of our approach for a flux solver is to transform the volume integrals of the source terms, which also contain the viscous fluxes, into surface integrals. This leads to non-homogeneous Rankine–Hugoniot conditions [15] at the corresponding cell interfaces, because the flux jump corresponds to the source added at a cell interface (Fig. 1b). If no source is added at the cell interface, homogeneous Rankine–Hugoniot conditions apply (Fig. 1a). The remaining conditions to determine the states C_1 and C_2 on the left and right sides of a cell interface are provided by linearizing the characteristic relations. Thus, to compute the fluxes f_{C_1} and f_{C_2} at a cell interface, a nonlinear system for six unknowns has to be solved, where three equations come from the linearized Riemann invariants and three from the Rankine–Hugoniot jump conditions. Because of its

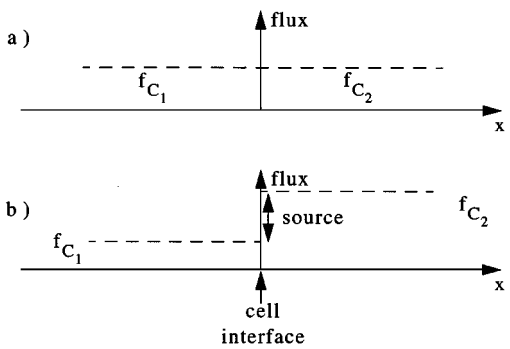

FIG. 1. Illustration of Rankine–Hugoniot conditions (a) homogeneous, flux jump equal zero; (b) non-homogeneous, flux jump equal source.

construction, we call the new non-homogeneous Riemann solver the "Rankine–Hugoniot–Riemann solver," in short "RHR solver." If f_{C_1} is used as right flux in the left cell and if f_{C_2} is used as left flux in the right cell, the source term is properly taken into account in the flux discretization. A steady 1D test case of a premixed laminar flame demonstrates that non-physical pressure peaks and non-constant mass flow profiles can be avoided with this approach. Further it is shown how the multidimensional effects can be taken into account using the RHR solver. Applying dimension decoupling it is possible to consider the differences of the fluxes in the other space dimensions as parts of the source terms. Thus the new solver becomes a multidimensional Riemann solver treating the cross fluxes in a physical way using the Rankine–Hugoniot jump conditions. Results of two dimensional Bunsen flames and of a 2D inviscid channel flow with injection show that the RHR solver leads to much more accurate results than a conventional Riemann solver. Further a 1D simulation of two colliding flames demonstrates that the new solver also works for unsteady flow. Finally a 2D simulation of acoustics flattening a wedge-shaped Bunsen flame to a semicircle shows at least qualitatively a good agreement with experimental measurements.

Further details on the derivation, analysis, and application of the new approach for a flux solver are presented in the Ph.D. thesis of the first author [10].

In Section 2 the non-homogeneous Euler equations are presented, which are used for our analysis. Section 3 indicates the motivation for this research. The new approach for a flux solver is presented in Section 4, and its extension to multi-dimensions is shown in Section 5. In Section 6 the accuracy of the inviscid terms in the steady state is discussed and in Section 7 the stability limits for the scheme are derived. A 1D non-homogeneous hyperbolic model system is used in Section 8 to study the spatial accuracy for systems. Simulations of a 2D homogeneous Euler test case are discussed in Section 9. Finally results of premixed laminar 1D flames and 2D Bunsen flames are presented in Section 9 (steady) and in Section 10 (unsteady with acoustics). Conclusions are given in Section 11.

2. THE NON-HOMOGENEOUS EULER EQUATIONS

For simplicity and without loss of generality the non-homogeneous 1D Euler system

$$\frac{\partial \mathbf{U}}{\partial t} + \frac{\partial \mathbf{f}}{\partial x} = \mathbf{S} \tag{1}$$

with

$$\mathbf{U} = \begin{pmatrix} \rho \\ \rho u \\ \rho E \end{pmatrix}, \qquad \mathbf{f} = \begin{pmatrix} \rho u \\ \rho u^2 + p \\ u(\rho E + p) \end{pmatrix}, \qquad \text{and} \qquad \mathbf{S} = \begin{pmatrix} R \\ M \\ Q \end{pmatrix}, \tag{2}$$

will be discussed in our first studies to explain the basic idea. The species continuity equations are not shown as it is only necessary to look at the global continuity equation. Later, when the extension to more dimensions will be explained, the 2D system

$$\frac{\partial \mathbf{U}}{\partial t} + \frac{\partial \mathbf{f}}{\partial x} + \frac{\partial \mathbf{g}}{\partial y} = \mathbf{S} \tag{3}$$

with

$$\mathbf{U} = \begin{pmatrix} \rho \\ \rho u \\ \rho v \\ \rho E \end{pmatrix}, \qquad \mathbf{f} = \begin{pmatrix} \rho u \\ \rho u^2 + p \\ \rho uv \\ u(\rho E + p) \end{pmatrix}, \qquad \mathbf{g} = \begin{pmatrix} \rho v \\ \rho uv \\ \rho v^2 + p \\ v(\rho E + p) \end{pmatrix}$$

and (4)

$$\mathbf{S} = \begin{pmatrix} R \\ M \\ N \\ Q \end{pmatrix}$$

will be used. The symbols ρ, u, v, p, and E denote the density, the x- and the y-components of the velocity, the pressure and the total energy per unit mass, respectively. R, M, N, and Q denote mass, x- and y-momentum, and total energy source rates. It is important to notice that the non-homogeneous Navier–Stokes equations can be treated as a non-homogeneous Euler system, if the viscous terms are considered as a part of the source term **S**.

3. MOTIVATION

We use the following simple 1D test case of a steady, premixed laminar flame [8] (Fig. 2) to show the motivation for this work. Using SI units, the reaction rate k of the one step mechanism $A \rightarrow B$ is

$$k = 8 \times 10^6 \exp\left(-\frac{7500}{T}\right), \tag{5}$$

where T is the temperature. The molecular weights W_A and W_B are 0.029085 kg/mole, the viscosity μ is 7×10^{-5} Ns/m^2, the Prandtl number $\mathrm{Pr} = (\mu c_p)/\lambda$, and the Schmidt number $\mathrm{Sc} = \mu/(D\rho)$ are 0.7 (λ is the thermal conductivity, D the diffusion coefficient, and c_p the specific heat at constant pressure), the formation enthalpy of species A and B is zero and $H_B^0 = c_p W_B$ 1500 K, respectively, where $c_p = 1000$ J/(kg K). The ratio of specific heats is $\gamma = 1.4$. At the inlet we have the mass fraction of species A $Y_A = 1$ and $T = 300$ K. Since $\rho_{\mathrm{in}} u_{\mathrm{in}}$ must be equal to $\rho_{\mathrm{out}} u_{\mathrm{out}}$ in the steady state, we add

$$\frac{\rho_{\mathrm{out}} u_{\mathrm{out}} - \rho_{\mathrm{in}} u_{\mathrm{in}}}{\rho_{\mathrm{in}} - \rho_{\mathrm{out}}}$$

to the velocity field after each time step. Thus the mass within the computational domain keeps conserved and the flame is forced to stay within the computational domain. At the outlet the pressure is set equal to 1×10^5 Pa.

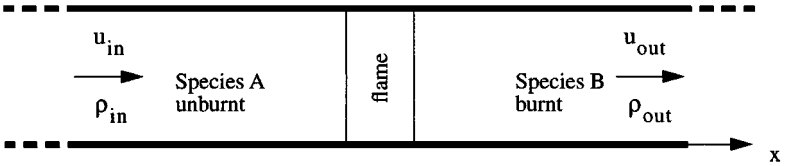

FIG. 2. The 1D test case of a steady, premixed laminar flame.

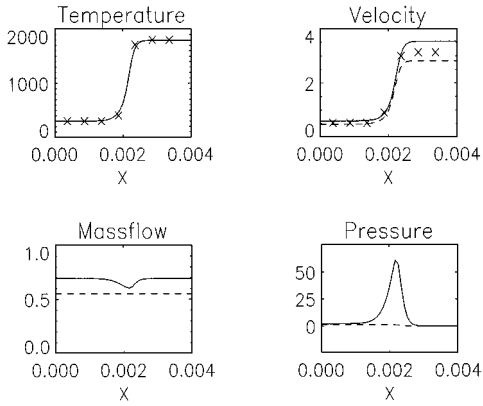

FIG. 3. Conventional Riemann solver (solid lines); RHR solver (dashed lines); [25] (markers).

The steady state results obtained on a grid with 50 equidistant mesh points with a conventional Riemann solver are presented in Fig. 3 (solid lines) where the temperature T, velocity u, mass flow ρu, and pressure $p - p_{\text{out}}$ profiles are shown in SI units. For simplicity a characteristic based Riemann solver (Subsection 4.1) was used. But the same phenomena can be observed if Roe's or an exact Riemann solver is applied. Although there is no source term in the global continuity equation and a conservative formulation has been used, the mass flow is not constant as it should be. Further a non-physical pressure peak in the flame zone of about 60 Pa can be observed which is about 400 times the dynamic pressure of the gas on the left side of the flame. To decrease these errors one could make an expensive grid refinement. The markers in the temperature and velocity plots show the result of an unsteady simulation on a mesh with 400 grid points [25].

The origin of these numerical phenomena, which can become much more dramatic in two or three space dimensions, can be found in the wrong flux evaluation at the cell interfaces when employing a conventional Riemann solver. In Subsection 4.2 the RHR solver is introduced which allows us to avoid the numerical errors and to produce correct results shown in Fig. 3 (dashed lines). The correct pressure distribution obtained with the RHR solver is enlarged in Fig. 4.

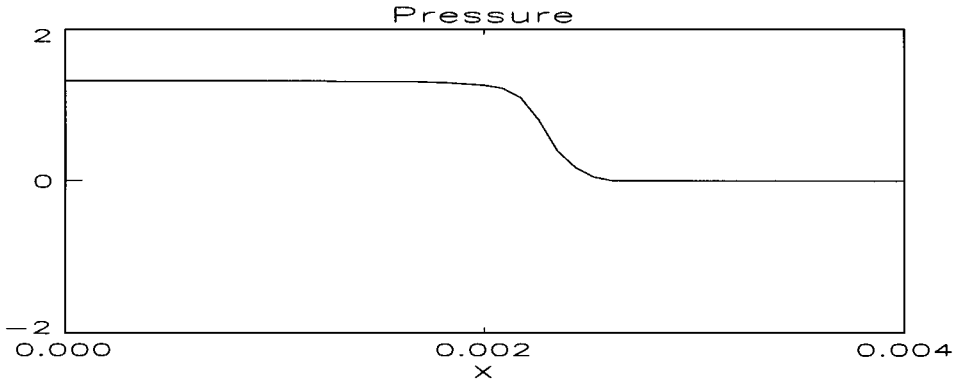

FIG. 4. $p - p_{\text{out}}$ with RHR solver.

In this paper the discretization of the inviscid terms is only first order in space. This does not influence the numerical phenomena qualitatively but it allows us to isolate the origin of the problems.

4. NEW APPROACH FOR A FLUX SOLVER

In Subsection 4.1 a characteristic based approximate Riemann solver is outlined. The Rankine–Hugoniot–Riemann (RHR) solver, which takes source terms and viscous fluxes into account, is introduced in Subsection 4.2. In Subsection 4.3, the RHR solver is illustrated for the linear advection equation.

4.1. *Characteristic Based Approximate Riemann Solver*

The characteristic based Riemann solver [27, 28] which is presented next works almost as well as an exact Riemann solver or an approximate one like Roe's for small Mach numbers, while for supersonic flow an exact Riemann solver or for example Roe's approximate Riemann solver are much better suited. For simplicity first order in space will be discussed. To achieve higher order in space the MUSCL ansatz [31] can be applied.

At the beginning of a time step constant values are assumed in the left and right cells $i-1$ and i of the cell interface $x_{i-1/2}$ (first picture in Fig. 5). These states in the areas A and B (third picture in Fig. 5) defining the Riemann problem are determined by the cell averages $\mathbf{U}_{i-1}^n$ and $\mathbf{U}_i^n$ in the cells $i-1$ and i at time $n\Delta t$. The second picture of Fig. 5 shows the approximate state after the time Δt where the expansion fan is approximated by a discontinuity. Here we assume 1D subsonic flow with $u_C > 0$. As soon as the states in the area C are known one can figure out the fluxes at the cell interface. The linearization of the

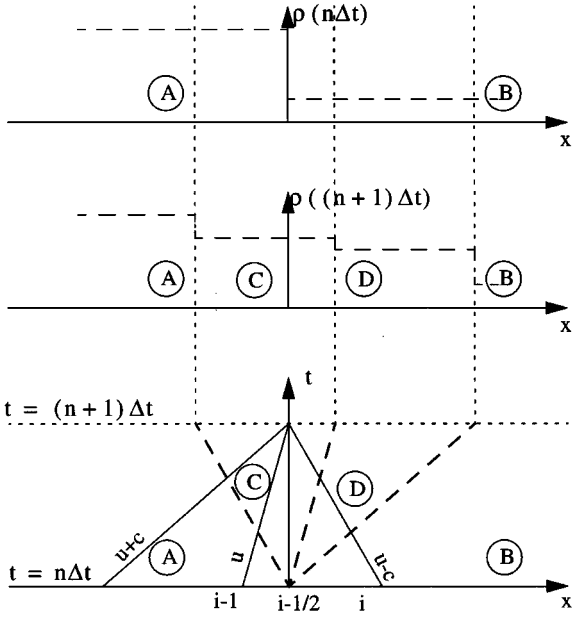

FIG. 5. Characteristic based approximate Riemann solver.

characteristic relations

$$\begin{aligned} c^2 d\rho - dp &= 0 \qquad \text{along the characteristic with the speed } u \\ \rho c du + dp &= 0 \qquad \text{along the characteristic with the speed } u + c \\ \rho c du - dp &= 0 \qquad \text{along the characteristic with the speed } u - c \end{aligned} \tag{6}$$

leads to the linear algebraic system (third picture in Fig. 5)

$$\begin{aligned} c_A^2\,(\rho_C - \rho_A) - (p_C - p_A) &= 0 \\ \rho_A c_A\,(u_C - u_A) + (p_C - p_A) &= 0 \\ \rho_B c_B\,(u_C - u_B) - (p_C - p_B) &= 0 \end{aligned} \tag{7}$$

which can be easily solved for ρ, u, and p in the area C [1]. This 1D approach is also used for multi-dimensions where u represents the velocity component normal to the cell interface. The velocity component parallel to the interface and the mass fractions, if more than one species are considered, are taken from the upwind side (region A in Fig. 5).

4.2. *Rankine–Hugoniot–Riemann* (*RHR*) *Solver*

The characteristic based approximate Riemann solver assumes hyperbolic homogeneous conditions. But if there is a source term, the assumption to have Riemann invariants is no longer valid, because the characteristic relations (6) will no longer be homogeneous.

The basic idea of our approach for a flux solver is to treat the source terms as surface integrals instead of volume integrals (Fig. 6). We consider 1D flow in a channel with height h. The parameter α_i is the fraction of the source terms in cell i distributed to the left interface. The distribution of non-negative fractions α_i and $1-\alpha_i$ to the left and right interfaces, respectively, requires α_i to be greater than or equal to zero and smaller than or equal to one. Thereby, the source term $h\Delta x(\alpha_i \mathbf{S}_i + (1-\alpha_{i-1})\mathbf{S}_{i-1})$ is located at the cell interface $x_{i-1/2}$, where $h\Delta x \mathbf{S}_i = h\Delta x \mathbf{S}(\mathbf{U}_i)$ approximates the volume integral of the source term $\mathbf{S}$ in cell i.

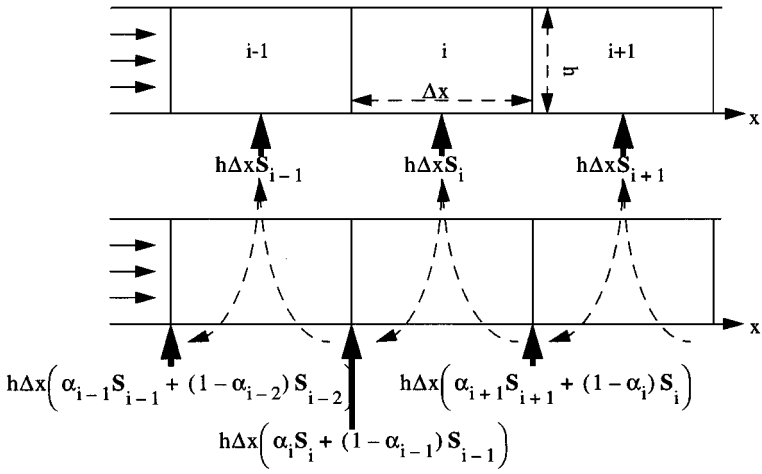

FIG. 6. Source terms distributed to cell interfaces.

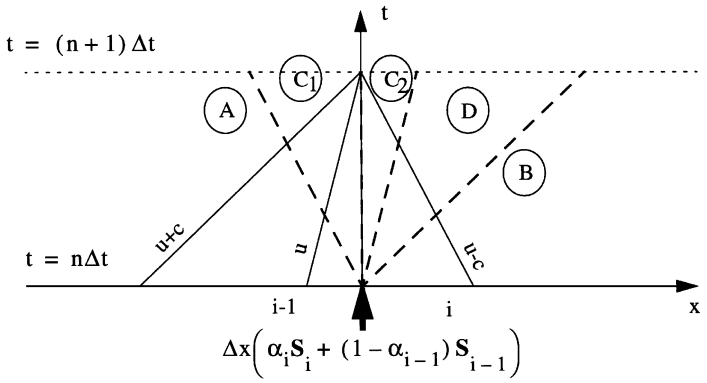

FIG. 7. Rankine–Hugoniot–Riemann (RHR) solver.

Thus one obtains piecewise homogeneous hyperbolic conditions in 1D with source terms as discontinuities at the cell interfaces.

In the characteristic diagram of Fig. 5 the source discontinuity at the cell interface would be located in the area C. Therefore it is necessary to divide C into the regions C_1 and C_2 (Fig. 7). During one time step constant states are assumed within the areas A, B, D, C_1, and C_2. Thus, the states in C_1 and C_2 are connected by the Rankine–Hugoniot jump conditions. These require the differences between the fluxes in C_1 and C_2 to be equal to the source terms located at the cell interface:

$$\begin{aligned}
(\rho u)_{C_2} - (\rho u)_{C_1} &= \Delta x(\alpha_i R_i + (1-\alpha_{i-1})R_{i-1}) \\
(\rho u^2 + p)_{C_2} - (\rho u^2 + p)_{C_1} &= \Delta x(\alpha_i M_i + (1-\alpha_{i-1})M_{i-1}) \qquad (8)\\
\left(\frac{\gamma}{\gamma-1}up + \frac{\rho}{2}u^3\right)_{C_2} - \left(\frac{\gamma}{\gamma-1}up + \frac{\rho}{2}u^3\right)_{C_1} &= \Delta x(\alpha_i Q_i + (1-\alpha_{i-1})Q_{i-1}).
\end{aligned}$$

Now the conditions are homogeneous and hyperbolic within the cells on both sides of the interface and the assumption of Riemann invariants along the characteristics becomes valid. Linearizing the characteristic relations (6) for the situation of Fig. 7 yields

$$\begin{aligned}
c_A^2(\rho_{C_1} - \rho_A) - (p_{C_1} - p_A) &= 0 \\
\rho_A c_A(u_{C_1} - u_A) + (p_{C_1} - p_A) &= 0 \qquad (9)\\
\rho_B c_B(u_{C_2} - u_B) - (p_{C_2} - p_B) &= 0.
\end{aligned}$$

Equations (8) and (9) constitute a nonlinear algebraic system for ρ, u, and p in the areas C_1 and C_2. Applying the Newton–Raphson method and using good start values (for example, those from the left and right cells at the time $t = n\Delta t$) one or two iterations are usually enough. Finally different fluxes for the left and right cells at the interface $i - 1/2$ are obtained with differences equal to $\Delta x(\alpha_i \mathbf{S}_i + (1-\alpha_{i-1})\mathbf{S}_{i-1})$.

Thus in 1D the only thing one has to do is to distribute the source terms and to replace the conventional Riemann solver by the RHR (Rankine–Hugoniot–Riemann) solver. Here we chose $\alpha = 0.5$ for the 1D simulations and for the 2D computations $\alpha = 1$, if the flow comes from the left side or from below, respectively. Thus, the source term is distributed to the upwind cell interface, if $\alpha = 1$ is chosen.

The sign of u, which is needed for the distribution of the source terms from the cell to the corresponding interfaces, is not known before the fluxes are computed. We have used the sign of u obtained with the characteristic based Riemann solver (7). For subsonic flow without source terms, there is no ambiguity in determining u_C in (7). We have chosen the following strategy: If the approximate cell interface velocities $u_{i-1/2}$ and $u_{i+1/2}$ are both positive (negative), $\alpha \Delta x \mathbf{S}_i$ is distributed to the upstream cell interface $x_{i-1/2}$ ($x_{i+1/2}$, respectively) and $(1-\alpha)\Delta x \mathbf{S}_i$ is distributed to the downstream cell interface $x_{i+1/2}$ ($x_{i-1/2}$, respectively). If $u_{i-1/2}u_{i+1/2} \le 0$ and not both $u_{i-1/2}$ and $u_{i+1/2}$ are zero, we set $\alpha_i = u_{i-1/2}/(u_{i-1/2} - u_{i+1/2})$ and $\alpha_i \Delta x \mathbf{S}_i$ and $(1-\alpha_i)\Delta x \mathbf{S}_i$ are distributed to the left and right cell interfaces, respectively. In that case, the distribution of the source term is biased towards the cell interface with the larger modulus of the cell interface velocity. If $u_{i+1/2} = u_{i-1/2} = 0$ we apply the characteristic based approximate Riemann solver to determine the momentum flux, i.e., $p_{i+1/2}$ and $p_{i-1/2}$.

It is important to notice that it is not necessary to store both fluxes $(\mathbf{f}_{C_1})_{i-1/2}$ and $(\mathbf{f}_{C_2})_{i-1/2}$, because

$$\left(\mathbf{f}_{C_2}\right)_{i-1/2} = \left(\mathbf{f}_{C_1}\right)_{i-1/2} + \Delta x(\alpha_i \mathbf{S}_i + (1-\alpha_{i-1})\mathbf{S}_{i-1}).$$

The update of the cell averaged variables can be done in the same way as with a conventional Riemann solver if either

$$\mathbf{f}_{i-1/2} = \left(\mathbf{f}_{C_1}\right)_{i-1/2} + \Delta x(1-\alpha_{i-1})\mathbf{S}_{i-1}$$

or (10)

$$\mathbf{f}_{i-1/2} = \left(\mathbf{f}_{C_2}\right)_{i-1/2} - \Delta x \alpha_i \mathbf{S}_i$$

is used as numerical flux and no additional variables have to be stored. For $u_{i-1/2} > 0$ the mass fractions $(Y_k)_{C_1}$ are given by $(Y_k)_{C_1} = (Y_k)_{i-1}$ and for $u_{i-1/2} < 0$ we use the relation $(Y_k)_{C_2} = (Y_k)_i$. In both situations the differences between the fluxes $\rho u Y_k$ in the areas C_1 and C_2 are equal to the corresponding source term discontinuities and Eq. (10) holds as for the other components of the flux vector $\mathbf{f}$.

The following equation shows an explicit Euler step:

$$\begin{aligned}\mathbf{U}_i^{n+1} &= \mathbf{U}_i^n + \frac{\Delta t}{\Delta x}\left(\mathbf{f}_{i-1/2}^n - \mathbf{f}_{i+1/2}^n\right) + \Delta t \mathbf{S}_i^n \\ &= \mathbf{U}_i^n + \frac{\Delta t}{\Delta x}\left(\underbrace{\mathbf{f}_{i-1/2}^n + \Delta x \alpha_i \mathbf{S}_i^n}_{\left(\mathbf{f}_{C_2}\right)_{i-1/2}^n} - \underbrace{\left(\mathbf{f}_{i+1/2}^n - \Delta x(1-\alpha_i)\mathbf{S}_i^n\right)}_{\left(\mathbf{f}_{C_1}\right)_{i+1/2}^n}\right). \qquad (11)\end{aligned}$$

The superscript n means that the values are taken at the time $t = n\Delta t$. For the time integration any other scheme can be applied. Here the explicit Euler method (11) is used, except for the stiff source terms of combustion which are treated implicitly according to $\mathbf{S}^{n+1} = \mathbf{S}^n + \partial \mathbf{S}^n / \partial \mathbf{U}'(\mathbf{U}'^{n+1} - \mathbf{U}'^n)$ with $\mathbf{U}' = (\rho_1, \ldots, \rho_{n_s})^T$. $\rho_1, \ldots, \rho_{n_s}$ denote the partial densities of n_s species. Notice that for simplicity the vector $\mathbf{U}'$ instead of $\mathbf{U}$ is used to derive

the Jacobian. This is much simpler and is good enough to stabilize the scheme. For the flux evaluation (10), the source terms are treated explicitly here.

The difference of the fluxes at the cell interfaces is exactly equal to the source term located there. That's the novel feature of our approach: we allow for different fluxes at a cell interface to accommodate the flux jump caused by adding mass, momentum, and energy via the source term at the cell interface. For explicit Euler time integration, we show with (11) that a conservative scheme is obtained if one uses the fluxes given in (10) for both sides of the volume interface. Therefore our scheme is conservative. Note that we obtain in (10) $f_{C_1} = f_{C_2} = f_C$, where state C is given by the characteristic based Riemann solver (Subsection 4.1), if $S = 0$.

At the beginning of a time step the viscous fluxes are computed at each cell interface, if the Navier–Stokes equations are solved. In each cell, the difference of the viscous fluxes over the right and left cell interfaces is added to the source terms. This is no modification for conventional flux solvers. But for the RHR solver it is, because the source terms are taken into account for the computation of the inviscid fluxes.

4.3. *RHR Solver for Nonhomogeneous Linear Advection Equation*

Let us consider the scalar 1D conservation law

$$\frac{\partial u}{\partial t} + \frac{\partial f(u)}{\partial x} = S \tag{12}$$

with the source term $S = S(x)$ independent of the conserved variable u. $f(u)$ is the flux function.

First, we are interested in the steady state

$$\frac{df(u(x))}{dx} = S(x). \tag{13}$$

Since we assume the characteristic speed $df(u)/du$ to be positive, we prescribe the boundary condition

$$u(x_a) = u_a \tag{14}$$

at the left boundary x_a. Integration of Eq. (13) yields

$$f(u(x)) = f(u_a) + \int_{x_a}^{x} S(\bar{x})\, d\bar{x}. \tag{15}$$

Assuming that the flux function f is invertible, we obtain the exact steady state solution

$$u(x) = f^{-1}\left(f(u_a) + \int_{x_a}^{x} S(\bar{x})\, d\bar{x} \right). \tag{16}$$

As an example, we consider the linear advection equation with a piecewise linear source term,

$$f(u) = au, \tag{17}$$

$$S(x) = \begin{cases} 0, & x_a \le x \le x_b \\ S_1(x - x_b), & x_b \le x \le x_c \\ S_1(x_d - x), & x_c \le x \le x_d \\ 0, & x_d \le x, \end{cases} \tag{18}$$

where a and S_1 are positive constants and $x_c - x_b = x_d - x_c$, i.e., $S(x)$ is continuous.

Let us consider the interval $[x_b, x_d]$ as cell i with cell interfaces $x_{i-1/2} = x_b$ and $x_{i+1/2} = x_d$. Suppose we distribute the exactly integrated source term $\Delta x S_i = \int_{x_{i-1/2}}^{x_{i+1/2}} S(x)\,dx$ to the upstream cell interface $x_{i-1/2}$. We obtain the RHR solver with $\alpha = 1$:

$$u_i^{n+1} = u_i^n - \frac{\Delta t}{\Delta x}\left[\left(au_{C_1}\right)_{i+\frac{1}{2}}^n - \left(au_{C_2}\right)_{i-\frac{1}{2}}^n\right]. \tag{19}$$

As u is a Riemann invariant on the characteristic $dx/dt = a$, we get

$$\left(u_{C_1}\right)_{i+1/2}^n = u_i^n \qquad \text{and} \qquad \left(u_{C_1}\right)_{i-1/2}^n = u_{i-1}^n$$

assuming a constant reconstruction, i.e., $u(x, n\Delta t) \approx u_i^n$ for x in $(x_{i-1/2}, x_{i+1/2})$, and the CFL condition $0 < a\Delta t/\Delta x \le 1$. The Rankine–Hugoniot condition yields

$$\left(au_{C_2}\right)_{i-\frac{1}{2}}^n = \left(au_{C_1}\right)_{i-\frac{1}{2}}^n + \Delta x S_i = au_{i-1}^n + \Delta x S_i.$$

Thus, (19) becomes

$$u_i^{n+1} = u_i^n - \frac{\Delta t}{\Delta x}\left[au_i^n - \left(au_{i-1}^n + \Delta x S_i\right)\right]. \tag{20}$$

This scheme corresponds to the first-order upwind method. In the steady state, we have the discrete form of (13):

$$\frac{au_i - au_{i-1}}{\Delta x} = S_i. \tag{21}$$

u_i^n corresponds to the exact steady state solution at $x = x_d$. If we reconstruct the cell average u_i^n as a constant function in cell i, we observe that the total flux jump over cell i is located at the upstream cell interface (Fig. 8).

For $\alpha = 1/2$, half of the source term is distributed to the left and right cell interfaces, respectively. The steady state fluxes are illustrated in Fig. 9. We see that in the steady state we have

$$\frac{au_i - au_{i-1}}{\Delta x} = \frac{au_{i+1} - au_i}{\Delta x} = \frac{1}{2}S_i. \tag{22}$$

u_i approximates the cell average better for $\alpha = 1/2$ than for $\alpha = 1$. In this particular example u_i is equal to the exact cell average

$$\frac{1}{\Delta x}\int_{x_{i-1/2}}^{x_{i+1/2}} u_{\text{exact}}(x)\,dx.$$

For the Burgers equation, i.e., $f(u) = u^2/2$ in (12), we obtain similar results with the RHR solver compared with the exact solution.

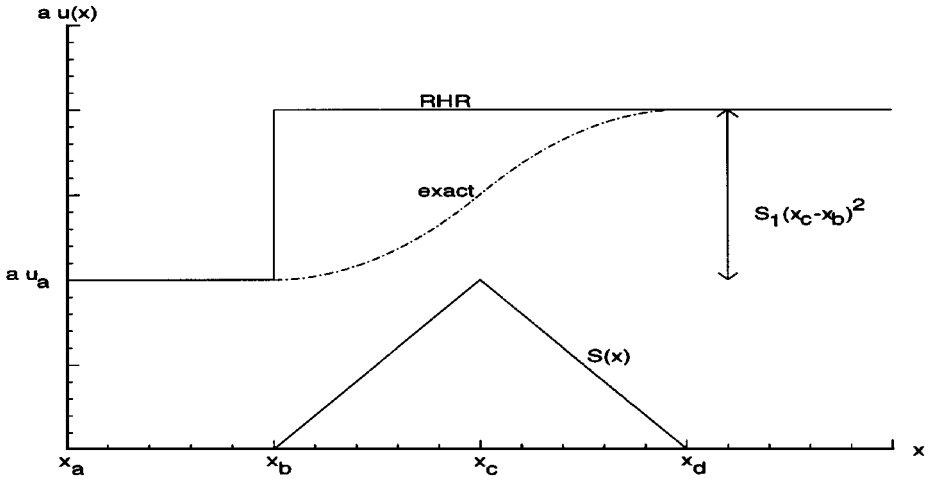

FIG. 8. RHR flux for $\alpha = 1$ and exact flux.

In the related approach by LeVeque [18,19], the total flux jump $\Delta x S_i$ is located at the cell center. The flow states in the left and right cell halves can be determined by the additional requirement of conservativity of u in a cell. The left and right states in all cells define homogeneous Riemann problems at the cell interfaces. Those are solved by a conventional Riemann solver.

In the steady state, the RHR solver satisfies the Rankine–Hugoniot condition

$$f(u_i) - f(u_{i-1}) = (1-\alpha)\Delta x S_{i-1} + \alpha \Delta x S_i. \tag{23}$$

If we assume u_i and u_{i-1} to approximate u at $x = x_{i-1/2} + \alpha\Delta x$ and $x = x_{i-1/2} - (1-\alpha)\Delta x$, respectively, relation (23) exactly holds for the exact steady state solution provided $\alpha = 1$ or $\alpha = 0$. For $0 < \alpha < 1$, relation (23) holds only approximately, unless the right hand side of (23) is equal to the integral of $S(x)$ from $x_{i-1/2} - (1-\alpha)\Delta x$ to $x_{i+1/2} + \alpha\Delta x$. Thus, the parameter α can also be interpreted as the fraction of the spatial increment in cell i

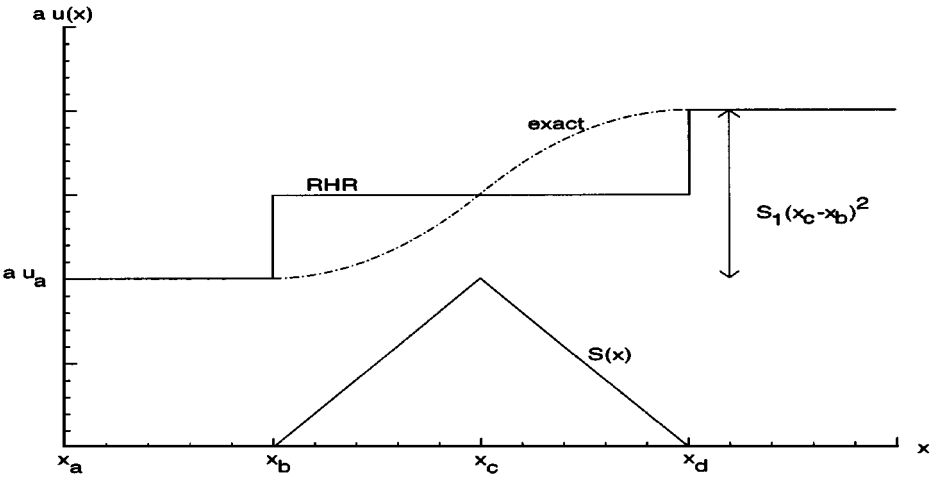

FIG. 9. RHR flux for $\alpha = 1/2$ and exact flux.

(i.e., $x - x_{i-1/2} = \alpha \Delta x$) where the conserved variable u is approximated by the cell average u_i to evaluate the flux $f(u_i)$.

Next, let us consider the steady state problem in a frame of reference moving with constant velocity $s < 0$ to the left. Suppose the initial condition corresponds to the steady state solution u_s. The exact solution reads

$$u(x,t) = u_s(x + st) - s. \tag{24}$$

If we solve the problem

$$\frac{\partial u}{\partial t} + (a - s)\frac{\partial u}{\partial x} = \tilde{S}(x,t) = S(x + st) \tag{25}$$

with the RHR solver, we obtain for the first time level

$$u_i^1 = u_i^0 - \frac{\Delta t}{\Delta x}\Big(\big((a-s)u_{C_1}\big)^0_{i+\frac{1}{2}} - \big((a-s)u_{C_2}\big)^0_{i-\frac{1}{2}} \Big). \tag{26}$$

Since

$$\big((a-s)u_{C_2}\big)^0_{i-1/2} - \big((a-s)u_{C_1}\big)^0_{i-1/2} = (1-\alpha)\Delta x S_{i-1} + \alpha \Delta x S_i,$$

$$\big(u_{C_1}\big)^0_{i-1/2} = u^0_{i-1} \qquad \text{and} \qquad \big(u_{C_1}\big)^0_{i+1/2} = u^0_i \qquad \text{for } 0 < (a-s)\Delta t/\Delta x \le 1,$$

we get

$$u_i^1 = u_i^0 - \frac{\Delta t}{\Delta x}\big((a-s)u_i^0 - \big((a-s)u^0_{i-1} + (1-\alpha)\Delta x S^0_{i-1} + \alpha \Delta x S^0_i\big)\big). \tag{27}$$

Because the discrete initial condition is assumed to correspond to the steady state solution $u_i^0 + s$ obtained with the RHR solver, the following relation holds

$$a u_i^0 - a u^0_{i-1} = a\big(u_i^0 + s\big) - a\big(u^0_{i-1} + s\big) = (1-\alpha)\Delta x S^0_{i-1} + \alpha \Delta x S^0_i. \tag{28}$$

Using (28) in (27) we get

$$u_i^1 = u_i^0 - \frac{\Delta t}{\Delta x}(-s)\big(u_i^0 - u^0_{i-1}\big). \tag{29}$$

Equation (29) is the first order upwind discretization of the linear advection equation

$$\frac{\partial u}{\partial t} - s\frac{\partial u}{\partial x} = 0 \tag{30}$$

which correctly describes the advection of u with the velocity $-s$. Also for the other scalar conservation laws and systems the RHR solver works consistently under Galilei-transformation.

For systems, the distribution of the integrated source term $\Delta x \mathbf{S}_i$ to the cell interfaces $x_{i\pm1/2}$ proceeds in the same way as for scalar conservation laws. The total integrated source term is distributed according to the velocity. Since the Rankine–Hugoniot conditions (8) are built into the numerical flux, the balance of flux difference and integrated source term is satisfied in the steady state. Unsteady motion is handled by the Riemann invariants at the cell interfaces.

For 1D non-homogeneous linear hyperbolic systems, the RHR solver with $\alpha = 1/2$ coincides with LeVeque's extension of Godunov's scheme [18] and Roe's source term treatment [24]. Even if the eigenvalues of the linear hyperbolic system have different signs and are different from zero, the RHR with any parameter $\alpha \in [0, 1]$ satisfies the Rankine–Hugoniot conditions in the steady state, whereas a conventional upwind scheme fails to do so (cf. Section 8). Note that the present approach for a flux solver differs from the ones by Roe [24] and LeVeque [18] in the nonlinear case.

5. EXTENSION TO MULTI-DIMENSIONS

In this section we show the analogy between source terms in 1D and multidimensional effects, if dimension decoupling is applied.

For simplicity a Cartesian 2D grid is used for the following investigations. It will be shown that it is possible to treat each row and each column of the grid in Fig. 10 as a 1D problem, if the approximation of the cross flow fluxes is good enough. The governing equations are the non-homogeneous 2D Euler equations (3) and (4).

To convert row j of the grid in Fig. 10 into a 1D problem it is necessary to replace the source terms $R_{i,j}$, $M_{i,j}$, $N_{i,j}$, and $Q_{i,j}$ by the modified source terms:

$$
\begin{aligned}
R_i^* &= R_{i,j} + \frac{(\rho v)_{i,j-1/2} - (\rho v)_{i,j+1/2}}{\Delta y} \\
M_i^* &= M_{i,j} + \frac{(\rho uv)_{i,j-1/2} - (\rho uv)_{i,j+1/2}}{\Delta y} \\
N_i^* &= N_{i,j} + \frac{(\rho v^2 + p)_{i,j-1/2} - (\rho v^2 + p)_{i,j+1/2}}{\Delta y} \\
Q_i^* &= Q_{i,j} \\
&+ \frac{((\gamma/(\gamma-1))vp + (\rho/2)v(u^2+v^2))_{i,j-1/2} - ((\gamma/(\gamma-1))vp + (\rho/2)v(u^2+v^2))_{i,j+1/2}}{\Delta y}.
\end{aligned}
\tag{31}
$$

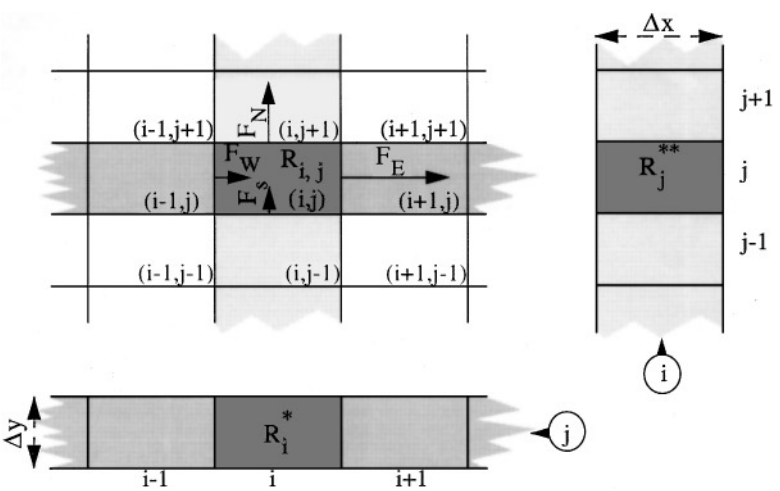

FIG. 10. Cross flow fluxes as source terms.

If the Navier–Stokes equations are solved, the source terms $S_{i,j}$ also contain the viscous flux balance. If this is done for all cells in row j the RHR solver presented in Subsection 4.2 can be applied to compute the fluxes at the interfaces $(1/2, j)$, $(3/2, j)$, $(5/2, j)$, etc. Equations (31), (9), $v_{C_1} - v_A = 0$, and $Y_{C_1} - Y_A = 0$ (if u is positive) form a nonlinear, but closed algebraic system for the primitive variables in the regions C_1 and C_2. For the fluxes $\rho u Y_k$, the mass fractions Y_k are taken from the upwind side (for positive u from the region A).

To compute the fluxes at the interfaces $(i, 1/2)$, $(i, 3/2)$, $(i, 5/2)$, etc., the same can be done for column i where the modified source terms

$$
\begin{aligned}
R_j^{**} &= R_{i,j} + \frac{(\rho u)_{i-1/2,j} - (\rho u)_{i+1/2,j}}{\Delta x} \\
M_j^{**} &= M_{i,j} + \frac{(\rho u^2 + p)_{i-1/2,j} - (\rho u^2 + p)_{i+1/2,j}}{\Delta x} \\
N_j^{**} &= N_{i,j} + \frac{(\rho u v)_{i-1/2,j} - (\rho u v)_{i+1/2,j}}{\Delta x} \\
Q_j^{**} &= Q_{i,j} \\
&+ \frac{((\gamma/(\gamma-1))up + (\rho/2)u(u^2+v^2))_{i-1/2,j} - ((\gamma/(\gamma-1))up + (\rho/2)u(u^2+v^2))_{i+1/2,j}}{\Delta x}
\end{aligned}
\tag{32}
$$

have to be used. This has to be done for all rows and columns. In our code the fluxes from the old time level are used to compute the modified source terms, i.e., the fluxes $(\,)_{i,j\pm1/2}$ in (31) and the fluxes $(\,)_{i\pm1/2,j}$ in (32). For the first time step 10 iterations are made starting with the fluxes obtained with a conventional Riemann solver.

In short one can describe the whole procedure as follows:

(i) The source terms have to be modified using (31) with the fluxes of the old time step. Note that $\mathbf{S}_{i,j}$ contains the viscous terms as well.

(ii) Because of stability reasons (see Section 7) the modification $\bar{\mathbf{S}}^*_{i,j} = (1-\theta)\mathbf{S}^*_{i,j} + \frac{\theta}{4}(\mathbf{S}^*_{i+1,j} + \mathbf{S}^*_{i-1,j} + \mathbf{S}^*_{i,j+1} + \mathbf{S}^*_{i,j-1})$ for the source terms is suggested. We have used $\theta = 0.04$ which is an empiric value.

(iii) Using $\bar{\mathbf{S}}^*_{i,j}$, the RHR solver can be applied to derive the fluxes at the eastern and western cell interfaces. We chose $\alpha_{i,j}$ equal to one, if u was positive at the interfaces $\partial\Omega_{i\pm1/2,j}$ and equal to zero, if u was negative at both interfaces. For $u_{i+1/2,j}u_{i-1/2,j} \le 0$ α was set equal to $u_{i-1/2,j}/(u_{i-1/2,j} - u_{i+1/2,j})$, if not both, $u_{i+1/2,j}$ and $u_{i-1/2,j}$, were zero. In that case $\bar{\mathbf{S}}^*_{i,j}$ was set equal to zero since then the RHR solver needs not to be applied.

(iv) Analogously to (i), (ii), and (iii), the northern and southern fluxes can be determined.

(v) These fluxes and the source term $\mathbf{S}_{i,j}$ are used for the time integration.

(vi) Goto (i) for next time step.

Modifications of the source terms are necessary to extend the RHR solver to axisymmetric flow with or without swirl, to flow in a rotating frame of reference, to 3D, and to structured meshes with curvilinear coordinates.

6. ACCURACY OF THE INVISCID TERMS IN THE STEADY STATE

We assume that in 1D the integral over the source terms (and the viscous terms) in cell i is accurate of order Δx^k, i.e., the error is $\beta_i \Delta x^k$. We define

$$\langle \beta \rangle = \frac{1}{N} \sum_{j=1}^{N} \beta_j \qquad \text{and} \qquad \Delta x = \frac{L}{N},$$

where L is a constant length scale and N is the number of cells. In the steady state the difference of the fluxes at $x_{i+1/2}$ and $x_{i-1/2}$ must be equal to the integral over the source term in cell i due to the conservativity of the scheme. Therefore, if the flux at $x_{1/2}$ is exact (e.g., if we have Dirichlet boundary conditions), the error of the flux at $x_{3/2}$ is $\beta_1 \Delta x^k$. By induction it follows that the errors of the fluxes at $x_{i+1/2}$ are

$$\Delta x^k \sum_{j=1}^{i} \beta_j$$

and at $x_{N+1/2}$ the expected error is

$$\Delta x^k N \langle \beta \rangle = \Delta x^k \frac{L}{\Delta x} \langle \beta \rangle = \Delta x^{k-1} L \langle \beta \rangle.$$

Since in the steady state the fluxes at the interface $x_{i+1/2}$ are equal to those in cell i if the RHR solver with $\alpha_i = 1$ is applied, the differences between the numerical steady state fluxes in cell i and the exact fluxes at $x_{i+1/2}$ are of order Δx^{k-1}. This has been demonstrated with a 1D Euler test case with a source term $Q(x)$ in the energy equation (Fig. 11; in units of $2.5 \times 10^5\,\mathrm{m^{-1}\,s^{-3}\,kg}$). The source term is a known function of x and can be exactly integrated over each cell. At the left boundary the velocity is 50 m/s and the temperature is 300 K. At the right boundary the pressure is 10^5 Pa. In the Figs. 11, 12, and 13 the velocity, temperature, and pressure profiles of the steady state solutions obtained on grids with 5, 10, 20, and 40 cells are shown. Figure 11 additionally shows the energy source term (in ordinate units of $2.5 \times 10^5\,\mathrm{m^{-1}\,s^{-3}\,kg}$). It can be observed that the cell averaged values are identical to the exact ones at the corresponding right cell interfaces.

For $0 \leq \alpha \leq 1$ the RHR solver guarantees that the fluxes in cell i lie between those at the corresponding interfaces, if the source term components do not change their sign within the cells i, $i+1$, and $i-1$. Therefore the fluxes in the cells are bounded by the fluxes at the interfaces. This is not the case with a conventional Riemann solver.

If steady state is obtained with a conventional Riemann solver, the fluxes and source terms are balanced for each cell, but for each additional time step shock tube problems have to be solved due to the jumps at the cell interfaces. This means that shocks, contact discontinuities, and expansion fans travel into the cells and by taking the average of the different regions in the cells at the end of the time step, numerical entropy is produced. This is a physical interpretation of numerical diffusion in 1D. The task is to make the jumps at the cell interfaces as small as possible which can be done by a higher order reconstruction of the flow variables at the left and right cell sides. Figure 14 shows the situation in 1D for the interface between the cells 2 and 3 for a conventional Riemann solver. It is shown that the flux differences $\Delta \rho u$ at the cell interfaces become smaller, if a second order MUSCL

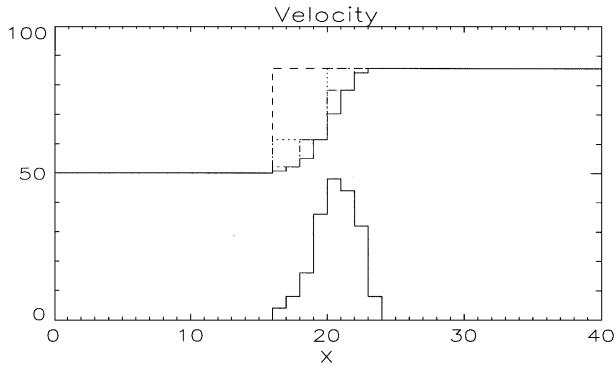

FIG. 11. Velocity plot of a 1D Euler test case with an exact source term (lower plot, in units of $2.5 \times 10^5\ s^{-3}\ m^{-1}\ kg$) in the energy equation on 4 different grids; 5, 10, 20, 40 cells: dashed, dotted, dash-dotted, solid lines.

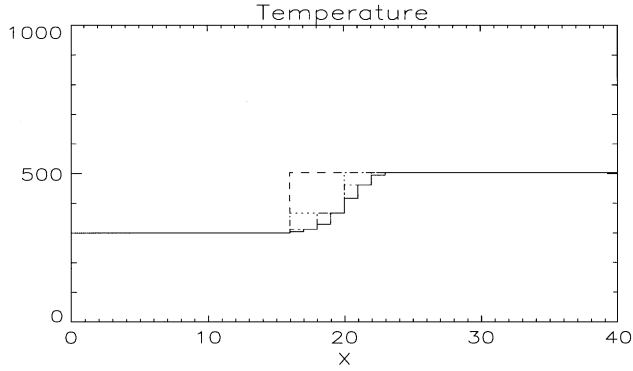

FIG. 12. Temperature plot of a 1D Euler test case with an exact source term in the energy equation on 4 different grids; 5, 10, 20, 40 cells: dashed, dotted, dash-dotted, solid lines.

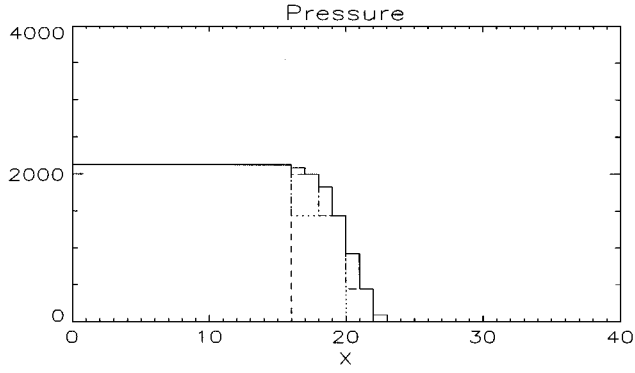

FIG. 13. Pressure plot ($p - p_\infty$) of a 1D Euler test case with an exact source term in the energy equation on 4 different grids; 5, 10, 20, 40 cells: dashed, dotted, dash-dotted, solid lines.

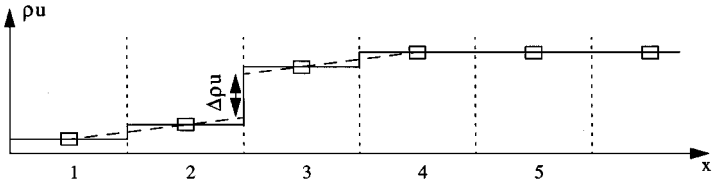

FIG. 14. Steady state obtained with a conventional Riemann solver.

scheme is applied. The situation is completely different in the steady state which is obtained with the RHR solver. Then the flux differences at the volume interfaces are equal to the source terms located there (and no shocks, contact discontinuities, or expansion fans travel into the volumes). After a further time step there is no mixing and therefore no numerical entropy production by the convective terms. Figure 15 shows this situation at the interface between the cells 2 and 3.

Figure 16 shows the spatial order of the flame velocity of the 1D test case of Section 3 (Fig. 3) using four different grids. It can be seen that the error $|u^{\text{num}}_{\text{flame}} - u^{\text{as}}_{\text{flame}}|$ ($u^{\text{as}}_{\text{flame}} = 0.522$ m/s is the flame velocity by [25]) depends on the flux solver and is of order one in all cases (conventional Riemann solver, RHR solver with $\alpha = 1$, and RHR solver with $\alpha = 0.5$), but more accurate with $\alpha = 0.5$. The fluxes are expected to be second order accurate and a possible reason for the first order of the flame velocity is that the volume averaged values (which is a first order approximation to the values at the volume interfaces; Figs. 11–13) are used for the evaluation of the viscous fluxes and the source terms.

7. STABILITY

First the stability condition for the scalar 1D model equation

$$\frac{\partial u}{\partial t} + a_1 \frac{\partial u}{\partial x} = -a_3 u, \tag{33}$$

where a_1 and a_3 are non-negative constants without viscous terms with the discretization (using the RHR solver with $0 \le \alpha \le 1$)

$$u_i^{n+1} = u_i^n - \frac{a_1 \Delta t}{\Delta x}\left(u_i^n - u_{i-1}^n\right) + (1-\alpha) a_3 \Delta t \left(u_i^n - u_{i-1}^n\right) - a_3 \Delta t u_i^{n+1} \tag{34}$$

will be derived. The third term on the right side of (34) corresponds to the second terms on the right side of the first equality of (10).

Note that the characteristic relations (9) simplify to $u_{C_1} = u_A$ for the 1D advection equation with $a_1 > 0$, and thus $(\mathbf{f}_{C_1})_{i-1/2} = a_1 u_{i-1}$ (cf. Subsection 4.3). For $\alpha = 1$, (34) is a first order upwind scheme.

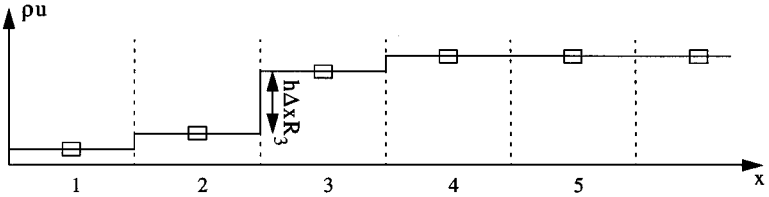

FIG. 15. Steady state obtained with the RHR solver.

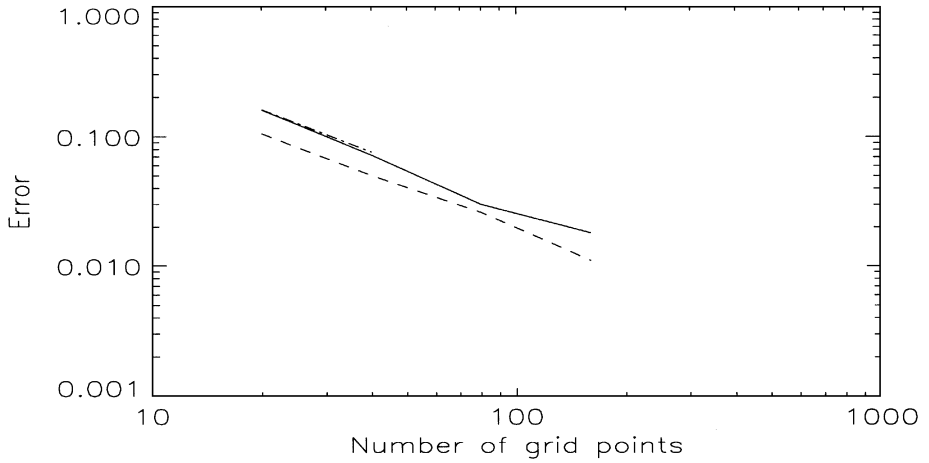

FIG. 16. Error $= |u^{\text{num}}_{\text{flame}} - u^{\text{as}}_{\text{flame}}|$; 20, 40, 80, and 160 points; $u^{\text{as}}_{\text{flame}} = 0.522\ \frac{\text{m}}{\text{s}}$; solid line, conventional Riemann solver; dashed line, RHR solver with $\alpha = 0.5$; dashed pointed line, RHR solver with $\alpha = 1$.

For (34) the von Neumann stability analysis leads to the sufficient stability conditions

$$\Delta t \leq \frac{\Delta x}{a_1 - \left(\frac{3}{2} - \alpha\right) a_3 \Delta x}, \qquad \text{if } (1-\alpha) a_3 \leq \frac{a_1}{\Delta x}$$

or (35)

$$\alpha \geq \frac{1}{2} - \frac{a_1}{a_3 \Delta x}, \qquad \text{if } (1-\alpha) a_3 \geq \frac{a_1}{\Delta x}.$$

To be sure to fulfill the second relation of (35) also for huge source terms a_3 and small wave speeds a_1 one has to choose $\alpha \geq 0.5$. If $\alpha = 1$ the first relation is equal to the time step restriction for an upwind scheme and for $\alpha < 1$ the restriction is even less stringent.

Next the 2D case will be studied. Therefore we consider the scalar equation

$$\frac{\partial u}{\partial t} + a_1 \frac{\partial u}{\partial x} + a_2 \frac{\partial u}{\partial y} = -a_3 u, \tag{36}$$

where a_1, a_2, and a_3 are non-negative constants with the following discretization (using the RHR solver with $0 \leq \alpha \leq 1$):

$$\begin{aligned} u^{n+1}_{i,j} = u^n_{i,j} &+ \Delta t \left(\frac{a_1}{\Delta x} u^n_{i-1,j} + (1-\alpha) \left(\frac{a_2}{\Delta y} u^n_{i-1,j-1} - \frac{a_2}{\Delta y} u^n_{i-1,j} - a_3 u^n_{i-1,j} \right) \right) \\ &- \Delta t \left(\frac{a_1}{\Delta x} u^n_{i,j} + (1-\alpha) \left(\frac{a_2}{\Delta y} u^n_{i,j-1} - \frac{a_2}{\Delta y} u^n_{i,j} - a_3 u^n_{i,j} \right) \right) \\ &+ \Delta t \left(\frac{a_2}{\Delta y} u^n_{i,j-1} + (1-\alpha) \left(\frac{a_1}{\Delta x} u^n_{i-1,j-1} - \frac{a_1}{\Delta x} u^n_{i,j-1} - a_3 u^n_{i,j-1} \right) \right) \\ &- \Delta t \left(\frac{a_2}{\Delta y} u^n_{i,j} + (1-\alpha) \left(\frac{a_1}{\Delta x} u^n_{i-1,j} - \frac{a_1}{\Delta x} u^n_{i,j} - a_3 u^n_{i,j} \right) \right) - \Delta t a_3 u^{n+1}_{i,j}. \end{aligned} \tag{37}$$

In Eq. (37) the terms corresponding to the second terms on the right side of the first equality of (10) are those with the factor $(1-\alpha)$. It is easy to see that we have a first order upwind

scheme if $\alpha = 1$. One part of that term consists of the flux difference of the cross fluxes which are taken here from the corresponding upwind cells. The numerical scheme which was used to produce the results presented in this work takes the cross fluxes from the old time level.

The von Neumann stability analysis leads to the sufficient stability conditions

$$\left.\begin{aligned} r_3 &\geq 1 + 2(r_1 + r_2) + 4r_4 \\ -r_3 &\leq 1 - 2(1-\alpha)(r_1 + r_2) \end{aligned}\right\} \quad \text{if } r_4 \geq -\min(r_1, r_2),$$

$$-r_3 \leq 1 + 2\alpha(r_1 + r_2) + 4r_4 \quad \text{if } r_4 \leq -\max(r_1, r_2),$$

where $r_1 = a_1 \Delta t/\Delta x$, $r_2 = a_2 \Delta t/\Delta y$, $r_3 = 1 + a_3 \Delta t$, and $r_4 = (1-\alpha)a_3 \Delta t - \alpha(r_1 + r_2)$. We investigate the two relations

$$r_3 \geq 1 + 2(r_1 + r_2) + 4r_4 \qquad \text{and} \qquad -r_3 \leq 1 + 2\alpha(r_1 + r_2) + 4r_4. \tag{38}$$

To satisfy the first condition of (38)

$$\alpha \geq \frac{1}{2} + \frac{a_3}{4}\left(\frac{a_1}{\Delta x} + \frac{a_2}{\Delta y} + a_3\right)^{-1} \tag{39}$$

must be fulfilled. For the second one we obtain the following stability limit for Δt:

$$\Delta t \leq \frac{\Delta x \Delta y}{\alpha(a_1 \Delta y + a_2 \Delta x) - (5 - 4\alpha)(1/2)a_3 \Delta x \Delta y}. \tag{40}$$

The relation (39) shows that α must be larger than or equal to 0.5. If the source term is huge ($a_3 \gg a_1/\Delta x + a_2/\Delta y$) α must be larger than or equal to 0.75. The conclusion is that in order to be sure to satisfy (39) one must set $0.75 \leq \alpha \leq 1$. If $\alpha = 1$, (37) becomes a classical upwind discretization of the corresponding differential equation with the stability condition (40).

8. SPATIAL ACCURACY FOR SYSTEMS

The numerical problem with the source term in one space dimension, which was the motivation for this work, is equivalent to finding characteristics for systems in multi dimensions. Generally it is not possible to diagonalize the Jacobian of the source term with the left and right eigenvector matrices of the Jacobian of the inviscid flux. In the scalar case, the Jacobians of the flux and of the source term are scalars and in diagonal form. Therefore these numerical phenomena cannot be studied with a scalar equation and a system has to be considered.

In Section 7 we have seen that the RHR solver with $\alpha = 1$ is equal to a first order upwind scheme and with $\alpha = 0$ we have a downwind discretization (for positive wave speeds). The RHR solver treats the source term in a different, physical way and we have seen in Section 5 that the fluxes of the other space dimensions can be treated as a part of the source term as

well. To study the non-scalar case we consider the one dimensional 2×2 system

$$\begin{aligned} \begin{pmatrix} \tilde{u} \\ \tilde{v} \end{pmatrix}_t + \underline{\mathbf{A}} \begin{pmatrix} \tilde{u} \\ \tilde{v} \end{pmatrix}_x &= -s \underline{\mathbf{Q}} \begin{pmatrix} \tilde{u} \\ \tilde{v} \end{pmatrix} \\ \underline{\mathbf{R}}^{-1} \begin{pmatrix} \tilde{u} \\ \tilde{v} \end{pmatrix}_t + \underline{\Lambda}\, \underline{\mathbf{R}}^{-1} \begin{pmatrix} \tilde{u} \\ \tilde{v} \end{pmatrix}_x &= -s \underline{\mathbf{R}}^{-1} \underline{\mathbf{Q}} \begin{pmatrix} \tilde{u} \\ \tilde{v} \end{pmatrix} \\ \begin{pmatrix} u \\ v \end{pmatrix}_t + \underline{\Lambda} \begin{pmatrix} u \\ v \end{pmatrix}_x &= -s \underline{\mathbf{R}}^{-1} \underline{\mathbf{Q}}\, \underline{\mathbf{R}} \begin{pmatrix} u \\ v \end{pmatrix} \end{aligned} \tag{41}$$

with the constant matrices $\underline{\mathbf{A}} = \underline{\mathbf{R}}\, \underline{\Lambda}\, \underline{\mathbf{R}}^{-1}$ and $\underline{\mathbf{Q}}$ with

$$\underline{\Lambda} = \begin{bmatrix} a & 0 \\ 0 & -b \end{bmatrix}, \qquad \begin{pmatrix} u \\ v \end{pmatrix} = \underline{\mathbf{R}}^{-1} \begin{pmatrix} \tilde{u} \\ \tilde{v} \end{pmatrix},$$

where a, b, u, and v are assumed to be positive and s is a function of x. The discretization with the RHR solver for the steady state

$$\underline{\Lambda} \begin{pmatrix} u \\ v \end{pmatrix}_x = -s \underline{\mathbf{R}}^{-1} \underline{\mathbf{Q}}\, \underline{\mathbf{R}} \begin{pmatrix} u \\ v \end{pmatrix}$$

leads to

$$\begin{aligned} &\begin{bmatrix} \frac{a}{\Delta x} & 0 \\ 0 & -\frac{b}{\Delta x} \end{bmatrix} \begin{pmatrix} u_i - u_{i-1} \\ v_i - v_{i-1} \end{pmatrix} \\ &\quad = -s_i \begin{bmatrix} \alpha' & 0 \\ 0 & \alpha'' \end{bmatrix} \underline{\mathbf{R}}^{-1} \underline{\mathbf{Q}}\, \underline{\mathbf{R}} \begin{pmatrix} u_i \\ v_i \end{pmatrix} - s_{i-1} \begin{bmatrix} \overline{\alpha'} & 0 \\ 0 & \overline{\alpha''} \end{bmatrix} \underline{\mathbf{R}}^{-1} \underline{\mathbf{Q}}\, \underline{\mathbf{R}} \begin{pmatrix} u_{i-1} \\ v_{i-1} \end{pmatrix}, \end{aligned}$$

where α' and α'' correspond to α of (34) and belong to the two characteristic equations of (41). In each equation of the characteristic form, $\overline{\alpha} = 1 - \alpha$ multiplied by the source term in the left cell of the interface has to be added to the upwind discretization of the fluxes. After the back transformation one obtains

$$\begin{pmatrix} \frac{\tilde{u}_i - \tilde{u}_{i-1}}{\Delta x} \\ \frac{\tilde{v}_i - \tilde{v}_{i-1}}{\Delta x} \end{pmatrix} = -s_i \underline{\mathbf{R}} \begin{bmatrix} \frac{\alpha'}{a} & 0 \\ 0 & -\frac{\alpha''}{b} \end{bmatrix} \underline{\mathbf{R}}^{-1} \underline{\mathbf{Q}} \begin{pmatrix} \tilde{u}_i \\ \tilde{v}_i \end{pmatrix} - s_{i-1} \underline{\mathbf{R}} \begin{bmatrix} \frac{\overline{\alpha'}}{a} & 0 \\ 0 & -\frac{\overline{\alpha''}}{b} \end{bmatrix} \underline{\mathbf{R}}^{-1} \underline{\mathbf{Q}} \begin{pmatrix} \tilde{u}_{i-1} \\ \tilde{v}_{i-1} \end{pmatrix}. \tag{42}$$

If $\alpha' = 1$ and $\alpha'' = 0$, then (42) is equal to the upwind steady state discretization:

$$\begin{pmatrix} \frac{\tilde{u}_i - \tilde{u}_{i-1}}{\Delta x} \\ \frac{\tilde{v}_i - \tilde{v}_{i-1}}{\Delta x} \end{pmatrix} = -s_i \underline{\mathbf{R}} \begin{bmatrix} \frac{1}{a} & 0 \\ 0 & 0 \end{bmatrix} \underline{\mathbf{R}}^{-1} \underline{\mathbf{Q}} \begin{pmatrix} \tilde{u}_i \\ \tilde{v}_i \end{pmatrix} - s_{i-1} \underline{\mathbf{R}} \begin{bmatrix} 0 & 0 \\ 0 & -\frac{1}{b} \end{bmatrix} \underline{\mathbf{R}}^{-1} \underline{\mathbf{Q}} \begin{pmatrix} \tilde{u}_{i-1} \\ \tilde{v}_{i-1} \end{pmatrix}. \tag{43}$$

For $\alpha' = \alpha'' = 0.5$ one obtains

$$\begin{pmatrix} \frac{\tilde{u}_i - \tilde{u}_{i-1}}{\Delta x} \\ \frac{\tilde{v}_i - \tilde{v}_{i-1}}{\Delta x} \end{pmatrix} = -\frac{s_i}{2} \underline{\mathbf{R}} \begin{bmatrix} \frac{1}{a} & 0 \\ 0 & -\frac{1}{b} \end{bmatrix} \underline{\mathbf{R}}^{-1} \underline{\mathbf{Q}} \begin{pmatrix} \tilde{u}_i \\ \tilde{v}_i \end{pmatrix} - \frac{s_{i-1}}{2} \underline{\mathbf{R}} \begin{bmatrix} \frac{1}{a} & 0 \\ 0 & -\frac{1}{b} \end{bmatrix} \underline{\mathbf{R}}^{-1} \underline{\mathbf{Q}} \begin{pmatrix} \tilde{u}_{i-1} \\ \tilde{v}_{i-1} \end{pmatrix}. \tag{44}$$

We consider the example

$$\underline{\mathbf{A}} = \begin{bmatrix} 0 & 1 \\ 2 & 1 \end{bmatrix} = \begin{bmatrix} 1 & -1 \\ 2 & 1 \end{bmatrix} \begin{bmatrix} 2 & 0 \\ 0 & -1 \end{bmatrix} \begin{bmatrix} 1/3 & 1/3 \\ -2/3 & 1/3 \end{bmatrix}, \qquad \underline{\mathbf{Q}} = \begin{bmatrix} 0 & 0 \\ 1 & 1 \end{bmatrix},$$

$$s = \begin{cases} 1 & \text{if } 0 \le x \le 1 \\ 0 & \text{else} \end{cases} \tag{45}$$

with $\tilde{v}(0) = \tilde{v}_0$ and $\tilde{u}(0) = \tilde{u}_0$. In the steady state we have

$$\tilde{v}_x = 0, \qquad \tilde{u}_x = \begin{cases} -\frac{\tilde{u}+\tilde{v}}{2} & \text{if } 0 \le x \le 1 \\ 0 & \text{else,} \end{cases}$$

and the exact solution is

$$\tilde{v} = \tilde{v}_0, \qquad \tilde{u} = \begin{cases} (\tilde{u}_0 + \tilde{v}_0)\, e^{-x/2} - \tilde{v}_0 & \text{if } 0 \le x \le 1 \\ \tilde{u}_0 & \text{if } x < 0 \\ (\tilde{u}_0 + \tilde{v}_0)\, e^{-1/2} - \tilde{v}_0 & \text{if } x > 1. \end{cases}$$

With the upwind discretization (43) ($\alpha' = 1, \alpha'' = 0$), $\Delta x = 1$, and $x_i = i - 1/2$ we have

$$\begin{aligned} &\begin{pmatrix} \tilde{u}_1 \\ \tilde{v}_1 \end{pmatrix} - \begin{pmatrix} \tilde{u}_0 \\ \tilde{v}_0 \end{pmatrix} = \frac{\tilde{u}_1 + \tilde{v}_1}{3} \begin{pmatrix} -0.5 \\ -1 \end{pmatrix} \Bigg\} \Rightarrow \frac{\tilde{u}_1 + \tilde{v}_1}{3} = \frac{2}{9}(\tilde{u}_0 + \tilde{v}_0) \\ &\begin{pmatrix} \tilde{u}_2 \\ \tilde{v}_2 \end{pmatrix} - \begin{pmatrix} \tilde{u}_1 \\ \tilde{v}_1 \end{pmatrix} = \frac{\tilde{u}_1 + \tilde{v}_1}{3} \begin{pmatrix} -1 \\ 1 \end{pmatrix} \\ &\quad \Rightarrow \begin{pmatrix} \tilde{u}_1 \\ \tilde{v}_1 \end{pmatrix} = \frac{1}{9} \begin{pmatrix} 8\tilde{u}_0 - \tilde{v}_0 \\ 7\tilde{v}_0 - 2\tilde{u}_0 \end{pmatrix}, \begin{pmatrix} \tilde{u}_2 \\ \tilde{v}_2 \end{pmatrix} = \frac{1}{3} \begin{pmatrix} 2\tilde{u}_0 - \tilde{v}_0 \\ 3\tilde{v}_0 \end{pmatrix} \end{aligned} \tag{46}$$

and with (44) ($\alpha' = \alpha'' = 0.5$),

$$\begin{aligned} &\begin{pmatrix} \tilde{u}_1 \\ \tilde{v}_1 \end{pmatrix} - \begin{pmatrix} \tilde{u}_0 \\ \tilde{v}_0 \end{pmatrix} = \frac{\tilde{u}_1 + \tilde{v}_1}{4} \begin{pmatrix} -1 \\ 0 \end{pmatrix} \Bigg\} \Rightarrow \frac{\tilde{u}_1 + \tilde{v}_1}{4} = \frac{\tilde{u}_0 + \tilde{v}_0}{5} \\ &\begin{pmatrix} \tilde{u}_2 \\ \tilde{v}_2 \end{pmatrix} - \begin{pmatrix} \tilde{u}_1 \\ \tilde{v}_1 \end{pmatrix} = \frac{\tilde{u}_1 + \tilde{v}_1}{4} \begin{pmatrix} -1 \\ 0 \end{pmatrix} \\ &\quad \Rightarrow \begin{pmatrix} \tilde{u}_1 \\ \tilde{v}_1 \end{pmatrix} = \frac{1}{5} \begin{pmatrix} 4\tilde{u}_0 - \tilde{v}_0 \\ 5\tilde{v}_0 \end{pmatrix}, \begin{pmatrix} \tilde{u}_2 \\ \tilde{v}_2 \end{pmatrix} = \frac{1}{5} \begin{pmatrix} 3\tilde{u}_0 - 2\tilde{v}_0 \\ 5\tilde{v}_0 \end{pmatrix}. \end{aligned} \tag{47}$$

The solid lines in the Figs. 17 and 18 show the exact steady state solutions of $\tilde{u}$ and $\tilde{v}$, while the dotted ones are the upwind solutions (46) with $\alpha' = 1$ and $\alpha'' = 0$ and the dashed lines those of (47) with $\alpha' = \alpha'' = 0.5$. For $\alpha' = 1$ and $\alpha'' = 0$ we observe a non-constant $\tilde{v}$ which is constant in the exact solution and in the solution with $\alpha' = \alpha'' = 0.5$. Further the solution of $\tilde{u}$ is much more accurate with $\alpha' = \alpha'' = 0.5$. We could show (Figs. 17 and 18) that the same phenomena of the combustion test case arise also in the steady state solution of this simple system and that the results become much better, if the source terms are distributed to the cell interfaces with the same weights.

The exact solution (bold lines), the numerical solution with $\alpha' = \alpha'' = 0.5$ (dashed lines), which corresponds to the RHR solution with $\alpha = 0.5$, and the numerical solution with $\alpha' = 1$ and $\alpha'' = 0$ (dotted lines), which is equal to a conventional upwind scheme, are shown. Opposed to the conventional upwind scheme, the RHR scheme captures the jump in $\tilde{u}$ and the constancy of $\tilde{v}$ correctly.

To avoid the numerical phenomena discussed above for the conventional upwind scheme, α must be equal for all equations. Further the von Neumann analysis for the RHR solver in 1D and 2D with the explicit Euler method for the time integration shows that the stability conditions for α (for positive u and v) are $0.5 \le \alpha \le 1$ in 1D (35) and $0.75 \le \alpha \le 1$ in 2D (39). In 1D, the RHR solver has proved to be more robust with $\alpha = 1$ than with $\alpha = 0.5$. To

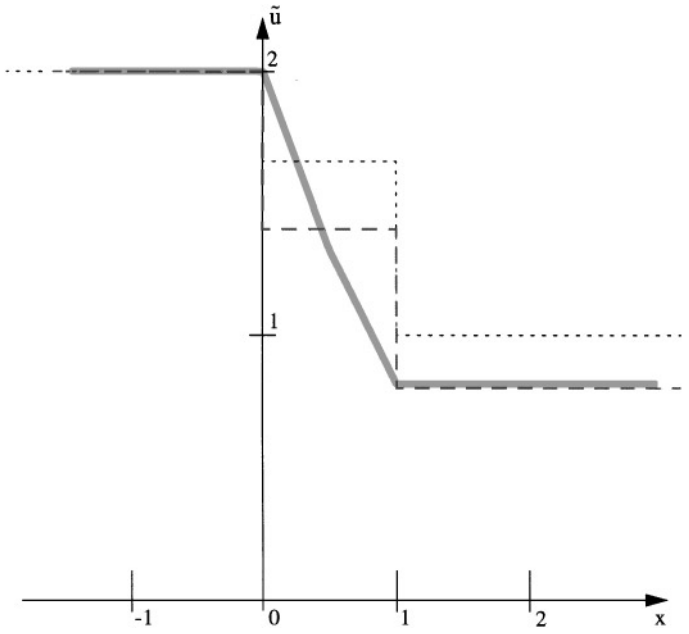

FIG. 17. Steady state solution $\tilde{u}$ of (46) and (47): exact solution (bold line); numerical upwind solution with $\alpha' = 1$ and $\alpha'' = 0$ (dotted line); and numerical solution with $\alpha' = \alpha'' = 0.5$ (dashed line).

overcome stability problems for 2D subsonic flow even with $\alpha = 1$, we used smoothed source terms (end of Section 5; for the time integration (11) the non-smoothed source terms are used) to compute the inviscid fluxes with the RHR solver (10).

9. RESULTS FOR STEADY FLOW

9.1. *1D Premixed Laminar Flame*

We consider the discussion of Section 3 for the 1D test case of a premixed laminar flame. The dashed lines in Fig. 3 show the steady state results obtained with the RHR solver with $\alpha_i = 0.5$ for the 1D flame test case introduced in Fig. 2. The solid lines in Fig. 3 show the

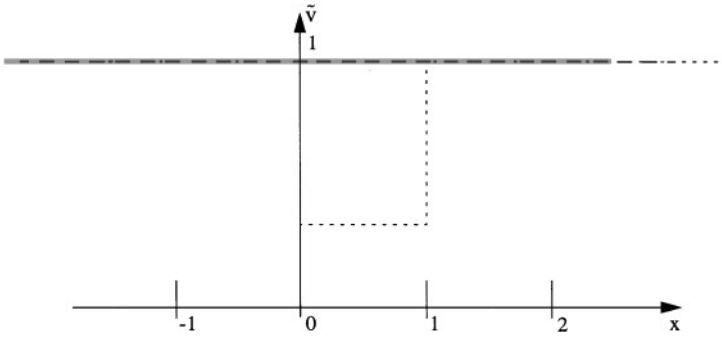

FIG. 18. Steady state solution $\tilde{v}$ of (46) and (47): exact solution (bold line); numerical upwind solution with $\alpha' = 1$ and $\alpha'' = 0$ (dotted line); and numerical solution with $\alpha' = \alpha'' = 0.5$ (dashed line).

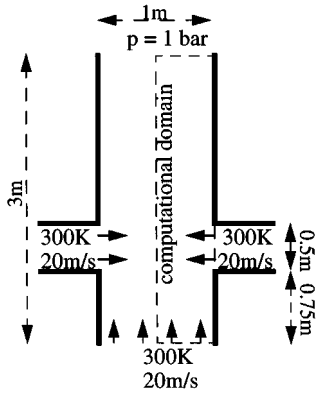

FIG. 19. The 2D Euler test case without source terms; injection in channel flow.

steady state results obtained with the characteristic based Riemann solver. The temperature plots are almost the same with the RHR and the characteristic based approximate Riemann solver. But with the RHR solver the mass flux is constant, no pressure peak can be observed and the flame velocity (i.e., $u(x=0)$) of the dashed plot is closer to the value by [25] which is about 0.522 m/s. In the pressure plot of Fig. 4, which is shown with another scale, a slight pressure decrease through the flame can be observed which corresponds to the Rankine–Hugoniot jump conditions.

Figure 3 shows that the RHR solver leads to much more accurate steady state results in 1D than a conventional Riemann solver.

9.2. *Injection in 2D Inviscid Channel Flow*

The new approach of a flux solver has been tested for the homogeneous compressible 2D Euler test case which is introduced in Fig. 19. A tube containing the main flow with inlets at the left and right walls where fluid is injected is considered. In shock free steady inviscid flow, the total pressure $p_0 = p(1 + ((\gamma-1)/2)M^2)^{(\gamma/(\gamma-1))}$ is constant along streamlines. Thus, the incompressible total pressure $p_{\text{tot}} = p + (u^2+v^2)\rho/2$, by which we approximate p_0 for low Mach number flow ($M_{\max} \approx 0.1$ here), is approximately constant along streamlines. The right plots of Fig. 20 show that this is fulfilled very well, if the RHR solver is used (an equidistant 16×26 grid was used for only one symmetry half). However, the result obtained with a conventional Riemann solver contains non-physical pressure peaks (left plots of Fig. 20) due to neglecting 2D effects. In Section 5 we showed the analogy between source terms in 1D and multidimensional effects if dimension decoupling is applied. This explains the non-physical solutions in homogeneous 2D Euler simulations (Fig. 20, left). The numerical error of conventional Riemann solvers reminds one of the carbuncle phenomenon in supersonic blunt body computations [22]. Taking 2D effects into account, our RHR solver computes the turning of the injected flow correctly (Fig. 20, right).

9.3. *2D Laminar Bunsen Flame*

The RHR solver also leads to more accurate solutions of the 2D combustion test case of Fig. 21 which shows an infinite series of laminar Bunsen flames. The same one step mechanism (5) of the 1D flame in Section 3 and Subsection 9.1 and a 16×21 grid were used (for one symmetry half only). Figure 22 shows the velocity vectors and the temperature

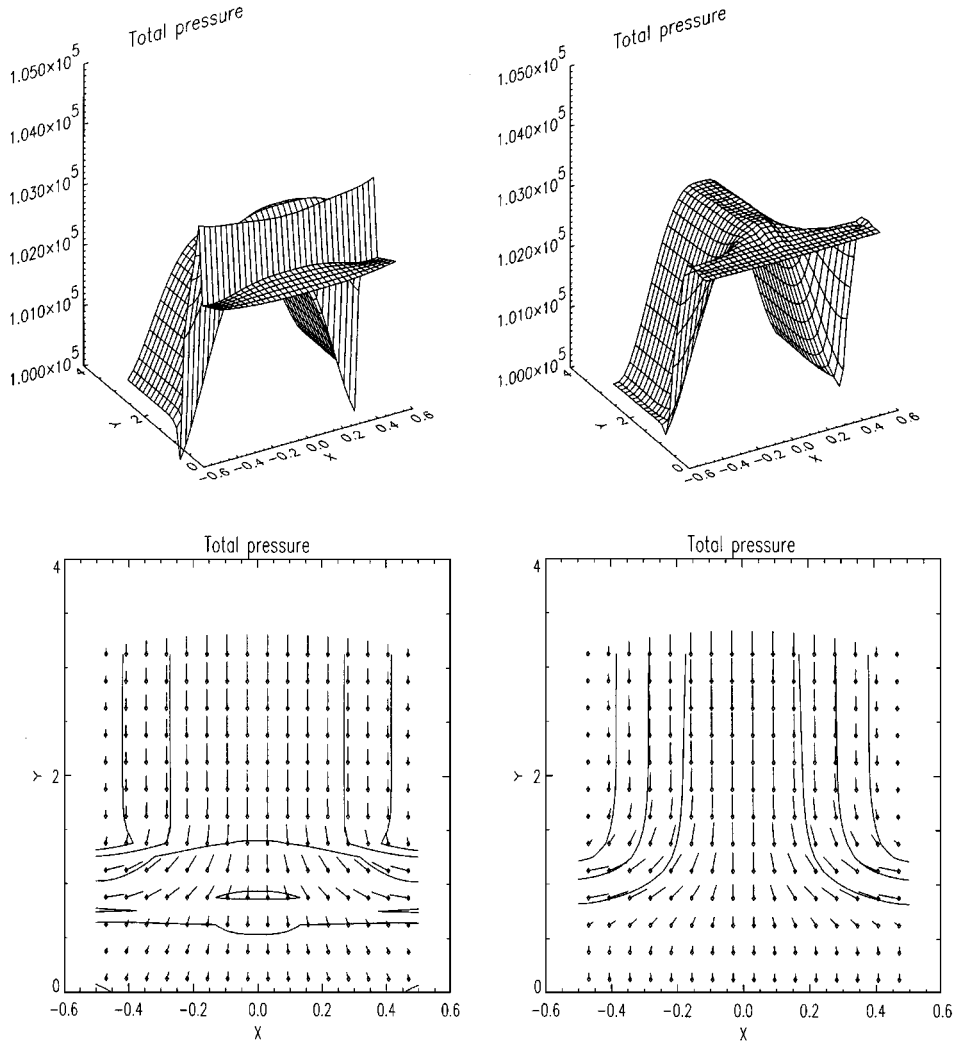

FIG. 20. Total pressure (surface and contour plots) and velocity field; RHR solver (right); conventional Riemann solver (left).

contour plots of the steady state results obtained with a conventional Riemann solver and with the RHR solver, respectively. The reactant mass fraction contours of the two solutions are plotted on top of each other in Fig. 23. The numerical flame shapes correspond very well to the approximate analytic solution of the flame contour (dashed lines; the numerical flame velocity of the 1D test case with 20 grid points was used). But already this figure shows some differences between the results. Much larger differences between the pressure fields $p - p_{\text{out}}$ of the two solutions are shown in Fig. 24. The same solutions are plotted from another view point and with different scales in Fig. 25. While the results obtained with a conventional Riemann solver (left plots of Figs. 24 and 25) show pressure differences of about 150 Pa the results obtained with the RHR solver show pressure differences of only 12 Pa (right plots of Figs. 24 and 25). The pressure decrease of about 2 Pa across the flame in Fig. 25 corresponds precisely to the results in Fig. 4 of the 1D test case. Additionally there is a global pressure decrease along the symmetry plane of the Bunsen flame due to

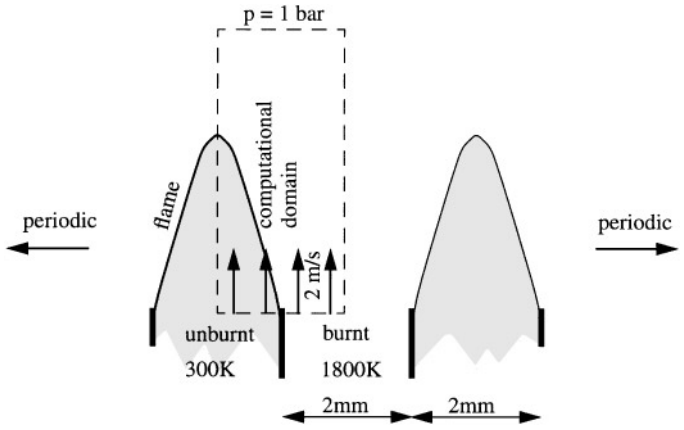

FIG. 21. The 2D combustion test case; an infinite series of Bunsen flames.

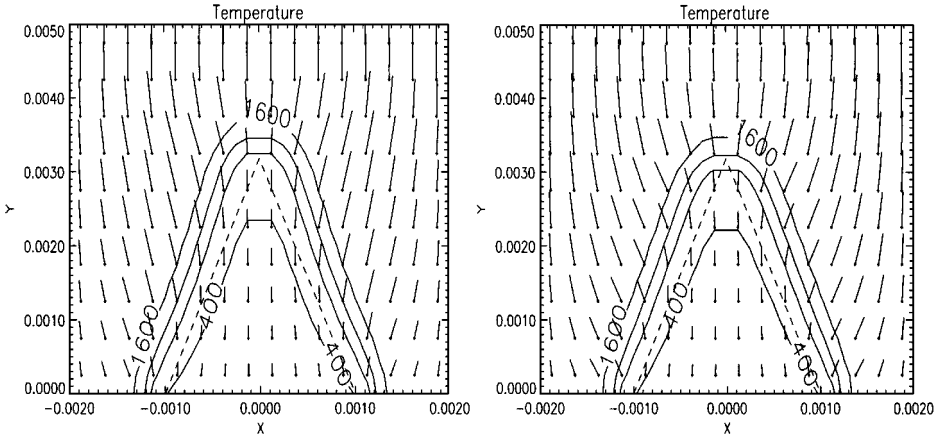

FIG. 22. Temperature contour plots with analytic solution and velocity field; RHR solver (right); conventional Riemann solver (left); approximate analytic solution (dashed lines).

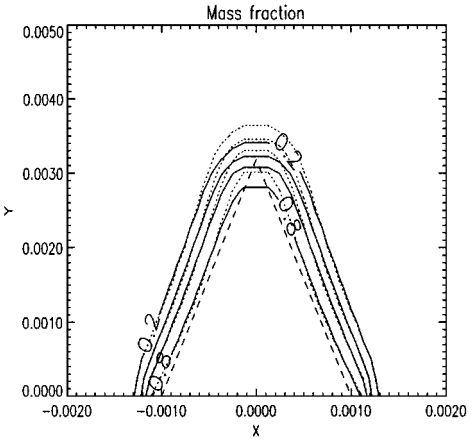

FIG. 23. Mass fraction contour plots with analytic solution; RHR solver (solid lines); conventional Riemann solver (dotted lines); approximate analytic solution (dashed lines).

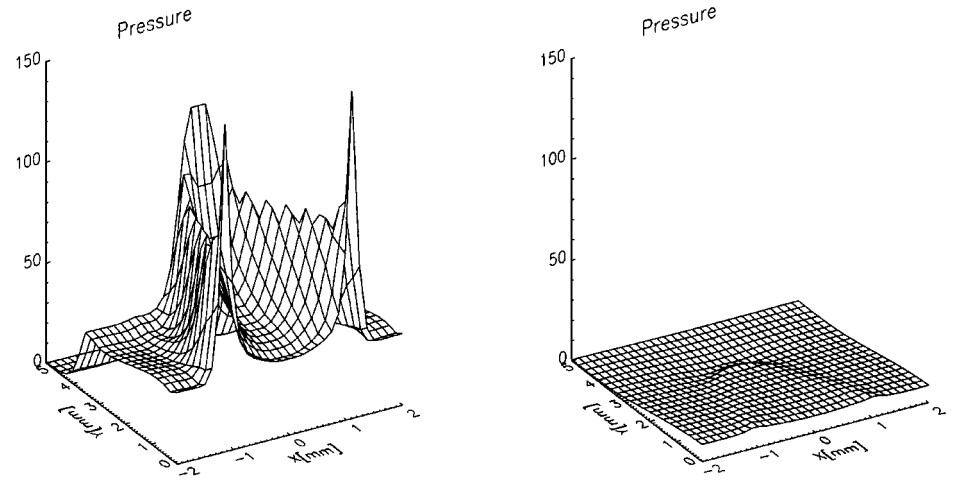

FIG. 24. Pressure surface plots; RHR solver (right); conventional Riemann solver (left).

the higher gas velocity at the top of the flame. If we notice that the pressure differences in the left plots of Figs. 24 and 25 are about 75 times the dynamic pressure of the unburnt gas at the bottom of the flame, it becomes clear that such large inaccuracies in the pressure field induce inaccurate streamlines and therefore the flame shape can become inaccurate. In Fig. 26 contour plots of u and v are shown. The right and left symmetry halves show the results obtained with the RHR solver and a conventional Riemann solver, respectively. Corresponding to the pressure fields, also their differences are considerable. Finally the pressure field, velocity vectors, and the reactant mass fraction contours of a simulation with far field boundary conditions at all boundaries (we have used Neumann boundary conditions) except for the unburnt gas at the southern inlet (Fig. 27) are shown in Fig. 28. Although the pressure and velocity fields differ very much from the solution of the test case with the infinite series of Bunsen flames, the flame shapes look similar.

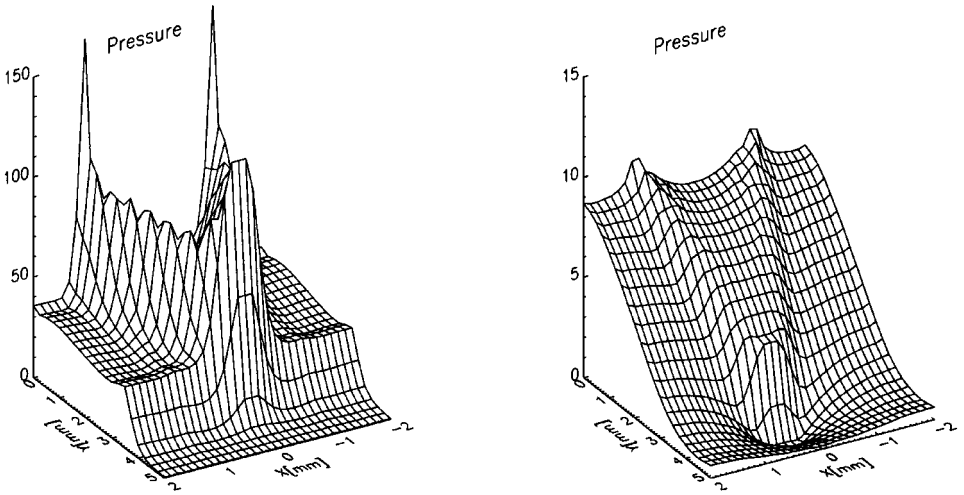

FIG. 25. Pressure surface plots; RHR solver (right); conventional Riemann solver (left).

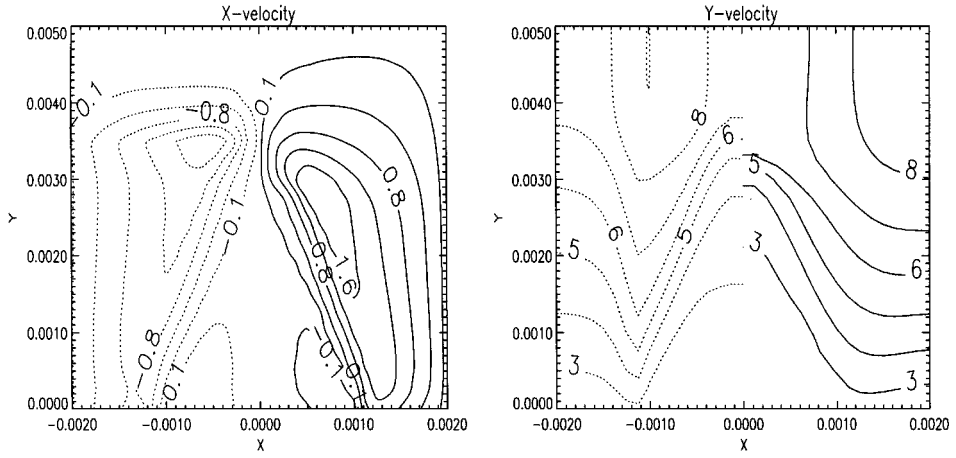

FIG. 26. Velocity (x-component: left; y-component: right) contour plots; RHR solver (solid lines); conventional Riemann solver (dotted lines).

It is even more important to obtain an accurate pressure field if acoustics in flames is to be studied and it is obvious that such huge errors as shown in the left plots of Figs. 24 and 25 will corrupt the results. It is possible to reduce these errors by a grid refinement but it is much cheaper to apply the RHR solver.

10. RESULTS FOR UNSTEADY FLOW

10.1. *Sound Generation by Colliding Flames*

The following 1D test case suggested by Professor G. Searby [26] shall demonstrate that the RHR solver allows us to make numerical studies of acoustics produced by two colliding flames in a tube. The same flame as in Fig. 3 was used but due to stability problems with $\alpha = 0.5$ the source term was distributed to the upwind side of the cell (for positive velocities to the left else to the right cell interface).

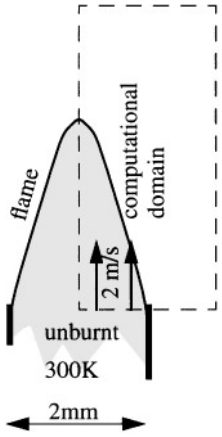

FIG. 27. The 2D combustion test case; far field boundary conditions.

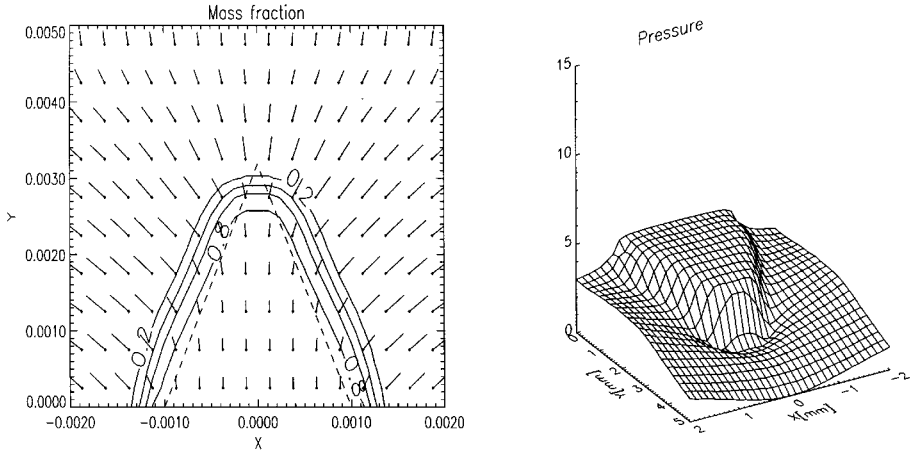

FIG. 28. Pressure field, mass fraction contours, and velocity vectors with far field boundary conditions using the RHR solver.

The collision of two flames in an infinitely long tube is studied. As the gradients at the boundary are assumed to be small, Neumann boundary conditions have been applied on **U** in order to have no reflections. The computational domain is the part of the tube where the collision of the flames takes place and is 2 mm long (only one-half of the symmetric field). The mesh has 25 grid points and the time step was 8×10^{-8} s (the maximum CFL number was about 0.8). In Fig. 29 the flames before the collision are sketched. They do not interfere yet, and the states in the areas on the left and right sides of the flames and between them are constant. After the collision (Fig. 30) two expansion waves travel away from the center with a constant speed u_{wave}, and the fluid between them is at rest. With the analytical solution derived in [10] one obtains 848.63 m/s for u_{wave}, 1793.15 K for T_{center} and -470.86 Pa for $p_{\text{center}} - p_\infty$, if the expansion waves are approximated by discontinuities.

With this we have a good estimate of the values in the center after the collision. To say more about the pressure during the collision the linear dependence of the acoustic pressure $p - p_\infty$ on $\dot{q}$ the rate of heat released in the domain [4, 26], is investigated. Thus, we check $p_{\text{center}} - p_\infty \approx c_1 \dot{q} + c_2$ where c_1 and c_2 are two constants. At the beginning $\dot{q}$ and the pressure in the center are constant. As soon as the preheat zones of the two flames interfere, the reaction rate and $\dot{q}$ grow and therefore the pressure level increases. After a while $\dot{q}$ becomes smaller because there is less and less fuel left until it is consumed at all. Then $\dot{q}$ is zero, and the pressure (p_{center}) remains constant.

Figure 31 shows the temperature, the velocity, and the mass fraction of the product at three different times. In Fig. 32 the pressure profiles $p - p_\infty$ at four different times are presented.

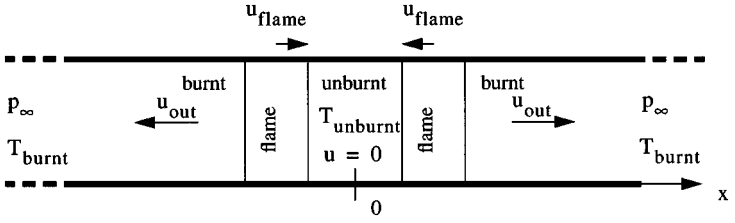

FIG. 29. Test case of two interacting flame fronts generating sound; before the collision.

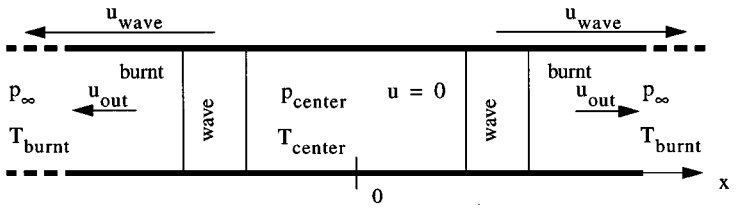

FIG. 30. Test case of two interacting flame fronts generating sound; after the collision.

To show that the simulation fulfills the criterion $p_{\text{center}} - p_\infty \approx c_1\dot{q} + c_2$, $p_{\text{center}} - p_\infty$, and $c_1\dot{q} + c_2$ with appropriate constants

$$c_1 = \frac{p_{\text{center}}(t=0) - p_{\text{center}}(t\to\infty)}{\dot{q}(t=0)} \qquad \text{and} \qquad c_2 = p_{\text{center}}(t\to\infty) - p_\infty$$

are shown in the same plot as a function of time (Fig. 33). As expected one can see only one curve. The difference $(p_{\text{center}} - p_\infty) - (c_1\dot{q} + c_2)$ is shown in Fig. 34. The numerical values in the center at the end of this simulation are -471.17 Pa for the pressure difference $p_{\text{center}} - p_\infty$ (the analytic value is -470.86 Pa) and 1793.11 K for the temperature (the analytic value is 1793.15 K). The velocity is zero as it should be. Thus the numerical results correspond almost precisely to the analytic ones.

10.2. *Oscillating Bunsen Flame*

The interaction of acoustic waves with a Bunsen flame was suggested by Professor G. Searby [6, 26]. At the same time we wanted to check whether the scheme with the RHR solver remains stable for this unsteady 2D computation.

The initial state was the steady 2D Bunsen flame with farfield boundary conditions of Fig. 27 but the velocity of the cold mixture at the outlet of the tube was 1.5 m/s and started

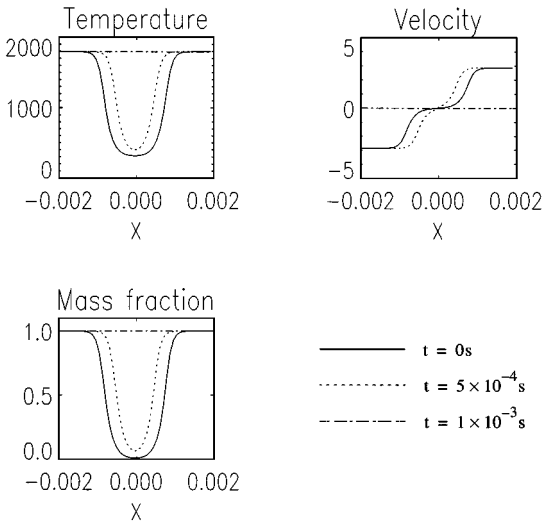

FIG. 31. Two interacting flame fronts generating sound in an infinitely long tube; temperature, velocity, and mass fraction plots at three different times.

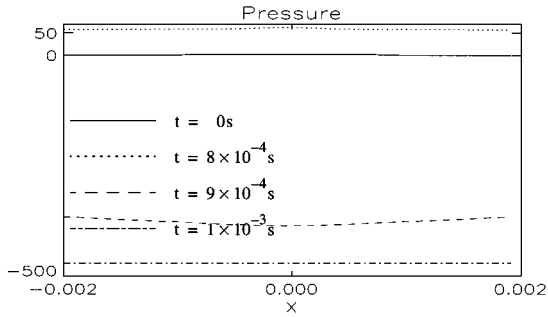

FIG. 32. Two interacting flame fronts generating sound in an infinitely long tube; pressure plots at four different times.

to oscillate at the time $t = 0$ s with a frequency of 10,000 Hz and an amplitude of 1 m/s (Fig. 35). Experiments by Hahnemann and Ehret [9] use a strong sound source located upstream in the tube and their measurements show that the flame contours are very close to sound potential surfaces. Figure 36 shows mass fraction isolines and velocity fields of our simulation at the times 0.014025, 0.01405, 0.014075, and 0.0141 s in the same plot (the isolines of the results at $t = 0.0141$ s are solid while the others are dotted). Additionally the isolines of the analytic solution of the sound potential surfaces [16, p. 378] are shown (dashed lines) and like in Hahnemann and Ehret's axisymmetric experiments one can see that near the plane of symmetry the flame contours are close to one of those semicircles. Figure 37 presents the pressure as a function of time which is periodic in time. The main differences between our numerical and Hahnemann and Ehret's experiments are first that our simulation was 2D and not axisymmetric like the physical experiments; second that the diameter of Hahnemann and Ehret's tube containing the reactive gas mixture was 5 times larger (i.e., 10 mm) than in our simulation; third that we have used a frequency of 10,000 Hz instead of about 5000 Hz; and fourth that the one step mechanism (5) might not properly describe the propane air combustion of the experiment. In our computation the flame was already flattened after about 5 oscillation cycles which could not be observed in Hahnemann and Ehret's experiments.

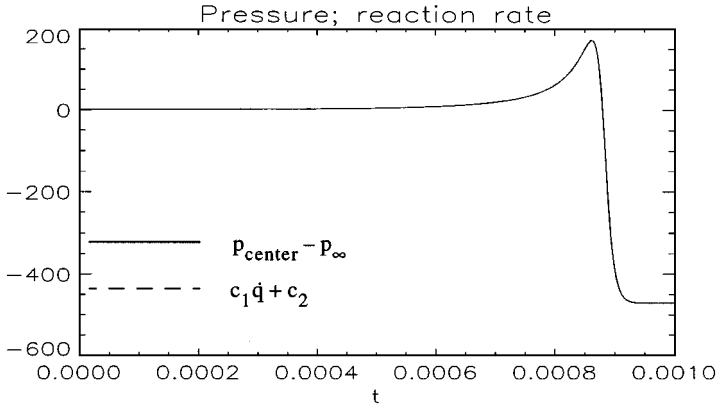

FIG. 33. Two interacting flame fronts generating sound in an infinitely long tube; pressure and heat release as functions of time.

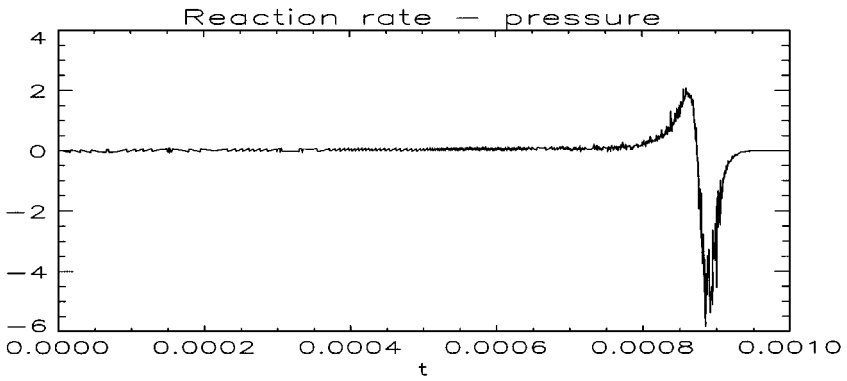

FIG. 34. Two interacting flame fronts generating sound in an infinitely long tube; $p_{\text{center}} - p_\infty - (c_1\dot{q} + c_2)$ as a function of time.

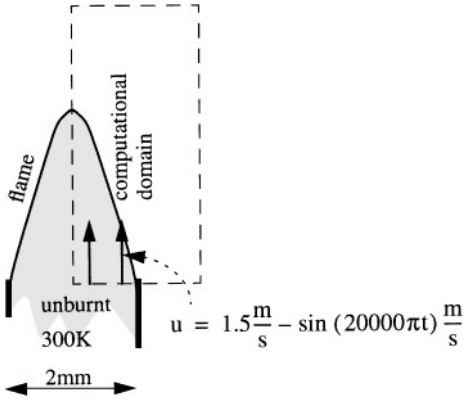

FIG. 35. Unsteady 2D combustion test case; oscillating Bunsen flame.

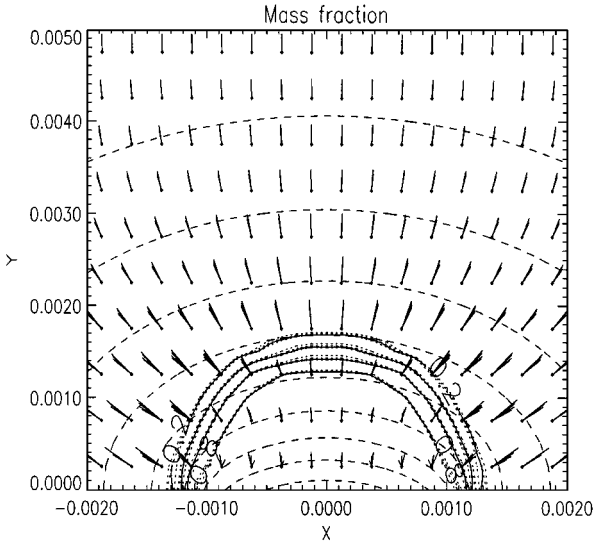

FIG. 36. Oscillating Bunsen flame at 4 different times within one oscillation; mass fraction contours and velocity vectors; analytic sound potential surfaces (dashed lines).

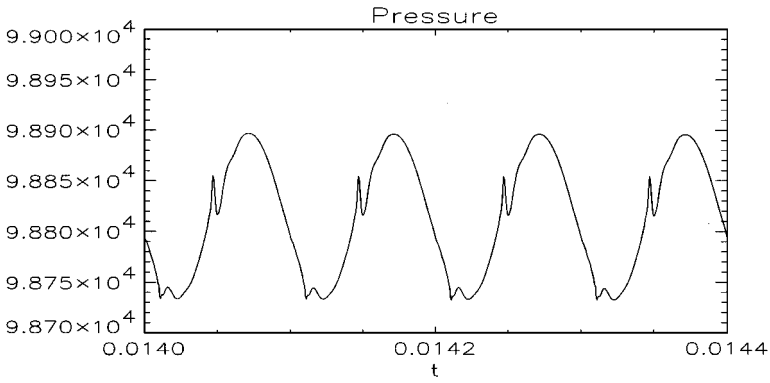

FIG. 37. Oscillating Bunsen flame: pressure at the nozzle as a function of time.

For higher velocities of the reactive mixture (e.g., 2 m/s instead of 1.5 m/s) no flattening of the flame could be observed but an oscillation with the acoustic frequency. Our physical interpretation of this phenomenon is the following: Since an acceleration field has a stabilizing effect on a premixed flame the flame tends to achieve the shape of an isopotential surface of the acoustic field. This is generally impossible because the total surface of the flame is almost constant for a given mean mass flow rate of the reactive gas mixture and the resulting flame shape is a compromise (Fig. 36). If the difference is too large, the flame cannot be stabilized by the acoustic acceleration field and will oscillate. This was also observed in the experiments by Hahnemann and Ehret [9]. Nevertheless, the situation there is different: Only a small change of the flame contour near the root is necessary to compensate the flame surface decrease due to change of the peak size. Therefore the axisymmetric flame can achieve a shape closer to an isopotential surface of the acoustic field than a flame in 2D.

For our simulation an equidistant Cartesian grid of 16×21 points (only one symmetry half) was used. One oscillation cycle corresponding to 1×10^{-4} s and 2000 time steps took approximately one hour on a SUN SPARC 20 workstation without any attempt to optimize the code.

11. CONCLUSIONS

A new approach for a flux solver which takes source terms, viscous terms, and multidimensional effects into account and its application to steady and unsteady simulations in 1D and 2D with and without combustion is presented. This work was motivated by a nonconstant mass flux and a non-physical pressure peak in steady 1D flame simulations. These errors originate in the assumption of Riemann invariants along the characteristics which is only valid for 1D homogeneous hyperbolic systems. The basic idea of the new solver is to distribute the source terms from the cells to the interfaces and treat them as discontinuities. Thus, one obtains hyperbolic conditions within the cells and the idea of Riemann invariants along the characteristics from the cells to the corresponding interfaces can be applied. Additionally the Rankine–Hugoniot jump conditions must be satisfied at the cell interfaces. Solving the nonlinear algebraic system consisting of three Rankine–Hugoniot conditions and three Riemann invariants leads to the RHR solver (Rankine–Hugoniot–Riemann solver). Since the laminar flame speed is a function of reaction rate, heat conduction, and molecular species diffusion, a minimum grid resolution is required. However, it has been shown that

a much finer grid is necessary for a conventional Riemann solver to keep the errors in the pressure field small (important for simulations of acoustics), whereas a much coarser grid can be used if the RHR solver is applied (cf. Figs. 3, 24, and 25). Opposed to other flux solvers the RHR solver allows us to make a physically based dimension decoupling if the flux differences of the other space directions are considered as a part of the source term. A 2D test case of an infinite series of laminar Bunsen flames shows that much more accurate results are achieved applying the new flux solver instead of a classical Riemann solver. For subsonic injection in a channel, a 2D Euler test case without source terms, the treatment of the 2D effects leads to a much more accurate total pressure field. An unsteady 1D test case of two colliding flames shows that the RHR solver allows us to simulate acoustics produced by combustion and an unsteady 2D test case demonstrates that it is possible to simulate the flattening of a Bunsen flame by an acoustic field. An open question concerns the stability of the multidimensional scheme with the RHR solver. For our 2D simulations a spatial smoothing of the modified source terms was necessary.

By modifying the source terms, the RHR solver can be extended to axisymmetric flow with or without swirl, to flow in a rotating frame of reference, to 3D, and to structured meshes with curvilinear coordinates.

This approach is more general and can be applied to solve other systems of partial differential equations which can be expressed as hyperbolic conservation laws with source terms.

ACKNOWLEDGMENTS

The authors thank Professor H. Thomann (ETH Zürich) for the valuable discussions and encouragement throughout the course of the present research and Professor G. Searby (I.R.P.H.E. Marseille) for suggesting and commenting on the test cases of Section 10.

REFERENCES

1. E. Becker, *Gasdynamik* (Teubner, Stuttgart, 1966).
2. A. Bermudez and M. E. Vazquez, Upwind methods for hyperbolic conservation laws with source terms, *Comput. & Fluids* **23**(8), 1049 (1994).
3. J. Chorin, Random choice methods with applications to reacting gas flow, *J. Comput. Phys.* **25**, 253 (1977).
4. P. Clavin, Premixed combustion and gasdynamics, *Ann. Rev. Fluid Mech.* **26**, 321 (1994).
5. P. Colella, Multidimensional upwind methods for hyperbolic conservation laws, *J. Comput. Phys.* **87**, 171 (1990).
6. D. Durox, F. Baillot, G. Searby, and L. Boyer, On the shape of flames under strong acoustic acceleration: A mean flow controlled by the unsteady flow, preprint, 1997.
7. H. A. Dwyer, Calculation of low Mach number reacting flow, *AIAA J.* **28**(1), 98 (1990).
8. G. Fernandez, K. Z. Tang, and H. A. Dwyer, A comparative study of the low Mach number and Navier–Stokes equations with time-dependent chemical reactions, in *Twelfth Int. Conference on Numerical Methods in Fluid Dynamics* (Springer-Verlag, Berlin, 1990), p. 490.
9. H. Hahnemann and L. Ehret, Ueber den Einfluss starker Schallwellen auf eine stationär brennende Gasflamme, *Z. Tech. Phys.* **24**, 228 (1943).
10. P. Jenny, *On the Numerical Solution of the Compressible Navier–Stokes Equations for Reacting and Non-reacting Gas Mixtures*, Diss. ETH Nr. 12030, ETH Zürich, 1997.
11. P. Jenny, B. Müller, and H. Thomann, Riemann solver for compressible combustion codes, in *Proceedings of First International Symposium on Finite Volumes for Complex Applications*, edited by F. Benkhaldoun and R. Vilsmeier (Rouen, France, 1996), p. 705.

12. P. Jenny, B. Müller, and H. Thomann, Correction of conservative Euler solvers for gas mixtures, *J. Comput. Phys.* **132**, 91 (1997).
13. J. J. Keller, Thermoacoustic oscillations in combustion chambers of gas turbines, *AIAA J.* **33**, 2280 (1995).
14. P. Klingenstein, *Nonlinear Hyperbolic Conservation Laws with Source Terms: Errors of the Shock Location*, Diss. ETH Nr. 12019, ETH Zürich, 1997.
15. K. K. Kuo, *Principles of Combustion* (Wiley, New York, 1986).
16. L. D. Landau and E. M. Lifschitz, *Hydrodynamik* (Akademie Verlag, GmbH Berlin, 1986).
17. R. J. LeVeque and H. C. Yee, A study of numerical methods for hyperbolic conservation laws with stiff source terms, *J. Comput. Phys.* **86**, 187 (1990).
18. R. J. LeVeque, Balancing source terms and flux gradients in high resolution Godunov methods, *J. Comput. Phys.*, in press.
19. R. J. LeVeque and D. Bale, Wave propagation methods for conservation laws with source terms, in *Proceedings of Seventh International Conference on Hyperbolic Problems, Zürich, Switzerland, 1998*.
20. D. Lindström, *Accurate Numerical Solution of Hyperbolic PDEs with Source Terms*, Dissertation, Uppsala University, 1996.
21. E. S. Oran and J. P. Boris, *Numerical Simulation of Reactive Flow* (Elsevier, New York, 1987).
22. J. J. Quirk, A contribution to the great Riemann solver debate, *Int. J. Numer. Methods Fluids* **18**(6), 555 (1994).
23. R. G. Rehm and H. R. Baum, The equations of motion for thermally driven buoyant flows, *J. Res. Natl. Bureau Standards* **83**, 297 (1978).
24. P. L. Roe, Upwind differencing schemes for hyperbolic conservation laws with source terms, in *Proceedings of Nonlinear Hyperbolic Problems*, edited by C. Carasso, P. A. Raviart, and D. Serre, Lecture Notes in Mathematics (Springer-Verlag, New York/Berlin, 1986), Vol. 1270, p. 41.
25. H. Scherer, *Numerische Simulation der Ausbreitung einer laminaren Vormisch-Flamme*, Semesterarbeit, Institut für Fluiddynamik, ETH Zürich, 1992.
26. G. Searby, Acoustic instability of laminar premixed flames, unpublished lecture notes, 1996.
27. J. Sesterhenn, B. Müller, and H. Thomann, A simple characteristic flux evaluation for subsonic flow, in *2nd ECCOMAS CFD Conf.* (Wiley, Chichester, 1994), p. 57.
28. J. Sesterhenn, *Zur numerischen Berechnung kompressibler Strömungen bei kleinen Mach-Zahlen*, Diss. ETH Nr. 11334, ETH Zürich, 1995.
29. P. K. Sweby, TVD schemes for inhomogeneous conservation laws, in *Nonlinear Hyperbolic Equations-Theory, Computational Methods and Applications*, edited by J. Ballmann and R. Jeltsch, Notes Numer. Fluid Mech. (Vieweg, Braunschweig, 1988), Vol. 24, p. 128.
30. E. F. Toro, *Defects of Conservative Methods and Adaptive Primitive Conservative Schemes for Computing Solutions to Hyperbolic Conservation Laws*, Technical Report MMU 9401, Department of Mathematics and Physics, Manchester Metropolitan University, 1994.
31. B. van Leer, Towards the ultimate conservative difference scheme. V. A second order sequel to Godunov's method, *J. Comput. Phys.* **32**, 101 (1979).
32. M. E. Vazquez, An efficient upwind scheme with finite volumes of the edge-type for the bidimensional shallow water equations, in *Proceedings of First International Symposium on Finite Volumes for Complex Applications*, edited by F. Benkhaldoun and R. Vilsmeier (Rouen, France, 1996), p. 605.